

2014

## Amine- and Sulfide-Sensing Copper(I) Iodide Films and the Structure, Dynamics, and Photophysics in the Copper(I) Iodide-Tetrahydrothiophene System

Kylie Marie Henline  
*College of William & Mary - Arts & Sciences*

Follow this and additional works at: <https://scholarworks.wm.edu/etd>

 Part of the [Inorganic Chemistry Commons](#), and the [Organic Chemistry Commons](#)

---

### Recommended Citation

Henline, Kylie Marie, "Amine- and Sulfide-Sensing Copper(I) Iodide Films and the Structure, Dynamics, and Photophysics in the Copper(I) Iodide-Tetrahydrothiophene System" (2014). *Dissertations, Theses, and Masters Projects*. Paper 1539626958.

<https://dx.doi.org/doi:10.21220/s2-j42s-fr15>

This Thesis is brought to you for free and open access by the Theses, Dissertations, & Master Projects at W&M ScholarWorks. It has been accepted for inclusion in Dissertations, Theses, and Masters Projects by an authorized administrator of W&M ScholarWorks. For more information, please contact [scholarworks@wm.edu](mailto:scholarworks@wm.edu).

Amine- and Sulfide-Sensing Copper(I) Iodide Films and the Structure,  
Dynamics, and Photophysics in the Copper(I) Iodide-Tetrahydrothiophene  
System

Kylie Marie Henline

Pittsburgh, PA

Bachelor of Science, Duquesne University, 2012

A thesis presented to the Graduate Faculty  
of the College of William and Mary in Candidacy for the Degree of  
Master of Science

Chemistry Department

The College of William and Mary  
May 2014

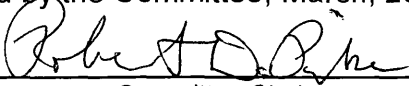
## APPROVAL PAGE

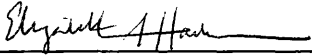
This thesis is submitted in partial fulfillment of  
the requirements for the degree of


Master of Science

  
Kylie Marie Henline

Approved by the Committee, March, 2014

  
Committee Chair  
Professor Robert Pike, Chemistry  
The College of William and Mary

  
Associate Professor Elizabeth Harbron, Chemistry  
The College of William and Mary

  
Assistant Professor William McNamara, Chemistry  
The College of William and Mary

## ABSTRACT

Volatile organic compounds (VOCs), detrimental to human health, are present in many household environments, necessitating novel methods of detection. Copper(I) iodide (CuI) is an inexpensive, commercial, air-stable salt that spontaneously reacts with a variety of VOCs to produce luminescent adducts, making CuI a good prospective detector material. Microcrystalline films of CuI have been cast from solution onto glass. As cast, the films show almost no visible emission; however, upon exposure to VOC amines and sulfides, the films form surface adducts that display a variety of visible emission colors. Chemically related VOCs produce remarkably different CuI-adduct emission colors in some cases. The films are reusable due to facile removal of the VOC. The surface of CuI films have been characterized using optical microscopy, scanning electron microscopy with energy dispersive spectroscopy, and powder X-ray diffraction. Limits of detection have been studied for specific VOCs by exposing CuI films and measuring their emission using an LED/fiber-optic fluorimeter. Tetrahydrothiophene (THT) produced a variety of luminescent adducts with CuI films. As a result, the CuI-THT system was studied more closely. Five new CuI-THT phases, four of which are luminescent, were structurally characterized using X-ray diffraction. These phases were further characterized using thermogravimetric and chemical analysis.



## TABLE OF CONTENTS

Acknowledgements	ii
List of Figures	iii
List of Tables	vii
Introduction	
Dangers of volatile organic compounds (VOC)	1
Luminescent detection	5
Copper(I) iodide	7
Hard-soft acid-base chemistry	9
CuI Complex Crystal Structures	10
Photophysics of CuI complexes	13
Experimental	
Materials	17
Instrumentation	17
Synthesis	25
Results and discussion	
CuI film characterization	31
CuI film VOC exposure luminescence results	41
CuI-L crystal structures	48
CuI-THT system	52
Conclusion	81
References	84

## ACKNOWLEDGEMENTS

I am forever indebted to Dr. Pike for his mentorship and guidance through my graduate career. My experience was fantastic due to his continuous support, encouragement, and contagious passion for science. I cannot thank him enough for the opportunity he gave me in working with him and all that he taught me. I would also like to thank Dr. Bebout, without whom, I would not have been able to join the graduate program at William and Mary. Her continuous support through my career was appreciated. Thank you also to my colleagues in Dr. Pike's research lab for all of their help and for making the lab a fun place to be. Special thanks go to Charles, who greatly assisted with my integration into my project. He taught me so much in the short time that we worked together and I am very grateful for his help.

My research would not have been possible without the assistance of many valued collaborators. I would like to thank Laura Rickard, Sean Koebley, and Dr. Hannas Schniepp for their assistance with optical microscopy and atomic force microscopy. I would also like to thank Samuel Hocker for teaching me to use the differential scanning calorimeter. For their help with Raman spectroscopy, I would like to give special thanks to Hannah Meyhew, Kristen Frano, and Dr. Wustholz. Thank you so much for your help not only collecting data but also analyzing it. I would also like to thank my undergraduate research advisor, Dr. Aitken, for allowing me access to her scanning electron microscope with energy dispersive spectroscopy and Kim Rosmus for her assistance in operating it. I am also grateful for the powder X-ray diffraction data provided by Andrew Kerr and Dr. Cahill at George Washington University. At the University of Maine I would like to thank John Ahern, Dr. Jim Killarney, and Dr. Patterson with their spectroscopic data and their assistance in understanding the photophysical data.

I would be remiss if I didn't also thank the Virginia Space Grant Consortium for their generous support which allowed me to travel to Atlanta for the SERMACS conference. I would also like to thank Jean Takeuchi for her generous gift which provides funding for the Kranbuehl-Thompson graduate fellowship. Thank you also to the National Science Foundation for their support as well.

Finally I would like to thank my fellow graduate students, past and present, for their friendship and support. I will miss them all dearly. Thank you also to the wonderful chemistry department staff and the laboratory directors for all of their help. I would like to thank my thesis committee, Dr. Pike, Dr. Harbron, and Dr. McNamara for the time they have devoted to my thesis. I would also like to thank my family for their unwavering support, love, and general awesomeness.

## LIST OF FIGURES

1. Schematic of a hot-bead pellistor-type combustible gas sensor	3
2. Design of potential inorganic luminescence-based VOC detector	6
3. Crystalline forms of CuI: (a) $\alpha$ -CuI, (b) $\beta$ -CuI, and (c) $\gamma$ -CuI	7
4. Phase diagram for crystalline forms of CuI	8
5. CuCN-L and CuSCN-L decorated chains, (a) (CuCN)(2-methylpyridine) <sub>1.5</sub> , (b) (CuSCN)(4-ethylpyridine) <sub>2</sub>	9
6. CuI-L common crystal structures (a) rhomboid dimer, (b) cubane tetramer, (c) stair step polymer. Cu: orange, I: purple, L: gray	11
7. CuI complexes with dithioether ligands: (a) cubane network and (b) chelated dimer. Cu: orange, I: purple, S: yellow, O: red, N: blue	12
8. Examples of CuI-sulfide ligand complexes: (a) cubane tetramer, (b) rhomboid dimer, and (c) a chelated 1-D stair step polymer	13
9. (a) Crystal structure of Cu <sub>4</sub> I <sub>4</sub> Py <sub>4</sub> (b) luminescence spectra of Cu <sub>4</sub> I <sub>4</sub> Py <sub>4</sub> : (i) spectrum at 295 K with an excitation wavelength of 380 nm, (ii) spectrum at 77 K with an excitation wavelength of 330 nm, (iii) spectrum at 77 K with an excitation wavelength of 365 nm	15
10. Luminescence response of CuCN powder after exposure to VOCs under 254 nm excitation	16
11. Spectrofluorimeter for measurement of inorganic substrate/VOC emission response. (A) LED controller, (B) LED source and filter enclosure, (C) fiber optic bundle, (D) sample chamber, (E) detector; inset: (F) inside view of sample chamber	23
12. Schematic of fiber optic bundle consisting of six outer fibers carrying 365 nm excitation light (blue circles) and one inner fiber carrying emission to the detector (red circle)	23

13. Spectrofluorimeter for measurement of inorganic substrate/VOC emission response in a flowing system. (A) Syringe pump, (B) mixing chamber for VOC and N <sub>2</sub> gas, (C) flow meter, (D) sample chamber, (E) outlet gas tubes, (F) LED controller, (G) LED source and filter enclosure, (H) fiber optic bundle, (I) detector, (J) Cul film	25
14. Vapor exposure chamber for Cul films	27
15. The doctor blade and micropipette used for film casting (right) and an optical microscopy image of a doctor blade cast Cul film (left)	31
16. Optical micrograph of doctor blade-cast Cul film (rendered using false colors)	32
17. Optical micrographs of evaporation-cast Cul films (rendered using false colors)	33
18. Optical micrographs of spin-coated Cul films, left: one coat, right: ten coats (rendered using false colors)	34
19. AFM micrographs of a single spin coated Cul film	34
20. SEM micrograph of doctor blade cast Cul films with Cu and I EDS hypermaps (upper right and lower right, respectively)	35
21. Raman spectrum of Cul films before (top) and after (bottom) Py exposure	37
22. Desk-top Raman spectra of the Cu <sub>4</sub> I <sub>4</sub> Py <sub>4</sub> and Cul solid exposed to Py	39
23. PXRD pattern of Cul film before and after exposure to saturated Py vapor	40
24. TGA traces for a Cul film before and after exposure to saturated Py vapor	41
25. VOC exposed Cul films under 365 nm excitation light	42
26. Ambient temperature luminescence spectra of Cul films after exposure to various VOCs	43
27. Ambient temperature luminescence spectra of Cul films after exposure to various VOCs	44

28. Ambient temperature luminescence spectra of CuI films after exposure to various VOCs	44
29. CuI film 15 min. 2-methylpyridine exposure using the static partial pressure-dependent fluorimetric analysis system at various partial pressures (saturation pressure of 2-methylpyridine is 10 Torr)	46
30. CuI film 15 min. pyridine exposure using the static partial pressure-dependent fluorimetric analysis system at various partial pressures (saturation pressure of pyridine is 20 Torr)	47
31. $(\text{CuI})_{\infty}(\text{2-bromopyridine})_{\infty}$ polymeric stair step crystal structure (right), packing diagram (left)	50
32. $(\text{CuI})_{\infty}(\text{2-chloropyridine})_{\infty}$ polymeric stair step crystal structure (right) and packing diagram (left)	52
33. Crystal structures of $(\text{CuI})_4(\text{Me}_2\text{S})_3$ (left) and $(\text{CuI})_4(\text{Et}_2\text{S})_3$ (right)	56
34. X-ray structure of $(\text{CuI})_4(\text{THT})_2$ , <b>1</b>	57
35. Thermal ellipsoid diagram for <b>1</b> (50% ellipsoids)	58
36. X-ray structure of $(\text{CuI})_{10}(\text{THT})_7(\text{MeCN})$ , <b>2</b> with Cu8 (90% occupancy)	60
37. X-ray structure of <b>2</b> (50% ellipsoids). Cu8-NCMe present at 90% occupancy and Cu9 (dashed) present at 10% occupancy	61
38. X-ray structures of $(\text{CuI})_4(\text{THT})_4$ polymorphs <b>3a</b> (left) and <b>3b</b> (one molecule only shown, right)	62
39. Thermal ellipsoid diagram of (a) <b>3a</b> and (b) <b>3b</b> (50% ellipsoids)	62
40. Wireframe overlay of <b>3a</b> (orange) and <b>3b</b> (green, one independent molecule only)	63
41. X-ray structure of $(\text{CuI})_3(\text{THT})_3 \cdot \text{MeCN}$ , <b>4</b>	64
42. Thermal ellipsoid diagram of <b>4</b> (50% ellipsoids)	64
43. Precipitate domains for CuI-THT in MeCN at various mixing ratios and temperatures	66

44. Photos of emissive phase CuI-THT powders under 365 nm excitation	66
45. Experimental and calculated PXRD patterns for complex <b>1</b>	68
46. Experimental and calculated PXRD patterns for complex <b>2</b>	69
47. Experimental and calculated PXRD patterns for complex <b>3a</b>	69
48. Experimental and calculated PXRD patterns for complex <b>3b</b>	70
49. Experimental and calculated PXRD patterns for complex <b>4</b>	70
50. Experimental and calculated PXRD patterns for complex <b>5</b>	71
51. TGA traces of CuI-THT phases	72
52. DSC trace for polymorphs <b>3a</b> (orange) and <b>3b</b> (green)	74
53. Luminescence spectroscopy of CuI-THT complexes at 293 K (top traces) and 77 K (bottom traces). Excitation wavelength (left) and emission wavelength (right) shown in each case. Dashed/solid line traces indicate linked excitation/emission pairs	77
54. 77 K emission spectra of luminescent CuI-THT complexes	78

## LIST OF TABLES

1. Examples of hard-soft acid-bases	10
2. Raman results for unexposed and exposed CuI films, and for solid Cu <sub>4</sub> I <sub>4</sub> Py <sub>4</sub> (room light peaks are excluded)	38
3. Crystal and structure refinement data for (CuI) <sub>∞</sub> (2-bromopyridine) <sub>∞</sub> and (CuI) <sub>∞</sub> (2-chloropyridine) <sub>∞</sub> .	48
4. Selected bond lengths (Å) and angles (°) for (CuI) <sub>∞</sub> (2-bromopyridine) <sub>∞</sub> and (CuI) <sub>∞</sub> (2-chloropyridine) <sub>∞</sub> .	50
5. Crystal and structure refinement data	53
6. Selected bond lengths (Å) and angles (°) for all CuI-THT complexes	55
7. Grinding and vacuum study results	75
8. Unit cell parameters for (CuI) <sub>4</sub> (THT) <sub>4</sub> cubane polymorphic phases	76
9. Luminescent behavior and lifetimes of the CuI-THT complexes	79

## INTRODUCTION

### Dangers of volatile organic compounds

Volatile organic compounds (VOCs) are a class of solid or liquid chemicals that emit vapor at room temperature. At sufficiently high concentrations, some VOCs can be harmful, making their detection vital to human safety in enclosed spaces where these high concentrations are often found. While acute VOC exposure is very dangerous, another concern is associated with chronic exposure resulting from the accumulation of VOCs indoors. VOCs are present in common household items such as paints, cleaning supplies, printers, office equipment, and furniture. Monitoring of VOCs is very important due to the ubiquitous occurrence of these potentially dangerous chemicals.<sup>1</sup> The adverse health effects of VOCs vary from minor to severe, depending on both concentration and the nature of the chemical hazard. Typical negative health effects from exposure to VOCs are eye, nose, and throat irritation, headaches, loss of coordination, nausea, and damage to liver, kidney, and nervous system.<sup>1</sup> Due to the dangerous nature of some VOCs, their detection is necessary to ensure the safety of individuals exposed to them.

The ideal VOC detector should be inexpensive, discriminating, portable, sensitive, and reversible. Reversibility means, in this instance, that the detector substrate is reusable. Detector portability is important for on-site analysis of VOCs. On-site analysis offers more immediate results, allowing for more rapid response, because there is no need to take samples to a laboratory for analysis.



This type of analysis also eliminates concerns about sample contamination or degradation because there is less sample handling and transportation. Despite the disadvantages noted above, off-site analysis often offers access to more reliable instrumentation. Although various techniques are available for VOCs detection, each of the current techniques has inherent limitations and weaknesses.

The choice of sensor required depends on the application. In some cases, a “general” sensor is sufficient. Such a device registers the concentration, or even merely a threshold alarm response for an aggregate of chemically-related analytes. Other applications may require a “specific” sensor which offers the identification and quantitation of one or more individual chemicals. An advantage of specific sensors is that they do not suffer from interference due to non-target compounds. Finally, there are many applications that require a sensor that features both general and specific characteristics, wherein multiple compounds in various chemical categories are quantified.

One currently available VOC detection strategy involves the use of electrochemical sensors.<sup>2</sup> Electrochemical sensors detect gaseous compounds by oxidizing them at an electrode and measuring the resulting current. Most of these sensors are substance-specific, but more general electrochemical sensors have also been developed. However, there are no electrochemical sensors available that are both general and compound-specific.

General detection strategies are of sufficient utility in the detection of combustible VOCs. The hot-bead pellistor, which is the most widely-used VOC detection technique, is an example of a combustible gas sensor.<sup>2</sup> A schematic showing how this type of sensor works is displayed in Figure 1. These sensors also work through oxidation of the substrate gas. This oxidation at the active bead produces heating which is proportional to the amount of gas in the air. The heating of the active bead corresponds to an increase in resistance which corresponds to the lower explosive limit (LEL) on the display screen of the sensor. LEL indicates the lowest concentration of combustible gas in the air capable of creating a flash fire in the presence of an ignition source.

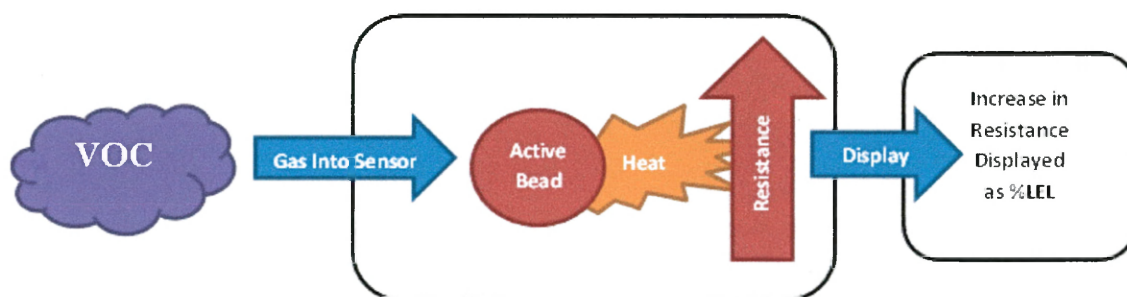


Figure 1. Schematic of a hot-bead pellistor-type combustible gas sensor

More sophisticated instrumental methods for VOC detection are also available. The two most widely used instruments for VOC detection are flame ionization (FID) and photoionization detectors (PID). As indicated by their names, both techniques rely on ionization of the VOCs in order to detect them. The difference between the two techniques lies in the method of ionization. Analyte ionization in an FID is caused by a hydrogen/air flame, while it is caused by ultraviolet light in PID.<sup>2</sup> A disadvantage associated with FID detectors is their

relative lack of portability. It is also often necessary to carry a heater with an FID system in order to heat the sample line to prevent VOCs from condensing in the transfer line.<sup>3</sup> The need for the heater and a source of compressed hydrogen make maneuvering around a site cumbersome. PID systems are much easier to transport than FID and are often used when portability is paramount or when FID is ineffective for detection of a particular VOC. Much like the hot-bead pellistors, these techniques show good generality, but lack specificity.

In fact, the only technologies available that combine compound-specificity and generality are mass spectrometry (MS), gas chromatography (GC), or the combined technique GC/MS. GC separates and quantifies compounds. MS identifies compounds based on fragmentation patterns. Combining GC and MS enables the separation with identification of compounds. GC/MS is therefore able to detect multiple VOCs while maintaining compound-specificity. Portability was once a major issue for GC/MS techniques because a vacuum is needed; but advances in the technology have made it increasingly simple to analyze air samples using either on-site or off-site strategies. Unfortunately, GC/MS systems are relatively expensive and require expertise to operate and analyze the data obtained.

Wolfrum et al. have reported a method that shows a promising combination of generality and specificity amongst several VOCs.<sup>4</sup> Wolfrum's "electronic nose" technology features an array of sensors and a method for processing the sensor response. In this technique, VOCs are measured using a heated metal oxide as the sensing component and partial least squares

regression for data processing. The latter is done by developing a multivariate calibration model based on the grouped sensor response. The sensing device in this study is capable of not only detecting and differentiating specific VOCs at sub-ppm concentration levels, but also quantifying them. The weakness associated with this detection method is that the calibration needed for these sensors would typically be too expensive and time-consuming.

Thus, while there are many techniques available for VOC detection, there remains a pressing need to develop systems that can both detect and differentiate between VOCs with low-cost and ease of use. The work described herein concerns VOC detection resulting from analyte adsorption by metal atoms. Metal centers have a well-known ability to spontaneously react with lone-pair bearing molecules. This ability can potentially be exploited in order to develop such a detection system.

### Luminescent Detection

The formation of a photoemissive adduct on an inorganic substrate could conceivably be used as a sensing strategy for the detection of VOCs in the air (Figure 2). An important feature of such a sensor is that the substrate should remain non-emissive under UV exposure and become emissive only after exposure to a VOC. UV light would serve the purpose of visualizing the detector response, and would not be necessary for the VOC adsorption to the detector film. For such a detection system to be practical the inorganic substrate should be castable as a film and the sensing device response should offer response that

is rapid, reversible, sensitive, and discriminating. Quick detector response is crucial when dangerous VOCs must be rapidly identified, for example in an industrial production facility. Sensitive sensors are also required when detecting VOCs that are harmful even at low concentrations. As discussed earlier, a combination of generality and compound-specificity is important depending on the application. Finally, (as noted above) reversible sensors are needed for cost-effectiveness. A sensor that can be reused will be less expensive to the consumer than one that is disposable. This feature would also make the detection system more environmentally friendly.

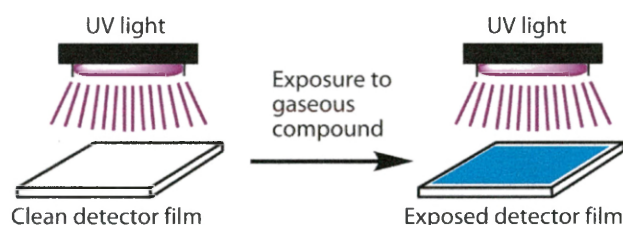


Figure 2. Design of potential inorganic luminescence-based VOC detector.

Luminescence spectroscopy is a potentially powerful basis for chemical detection due to its inherent high sensitivity. Through the use of light-emitting diode (LED), fiber optic, and miniaturized grating technologies, luminescence spectroscopy lends itself well to application in portable handheld devices. As described herein, the CuI-ligand system offers a diverse array of photoemissive adducts in which emission wavelength is dependent on the ligand (L) present. VOC-specific emission wavelength offers the potential for discrimination between various VOC adducts at the CuI surface which would combine generality and compound-specificity, a combination that is imperative to many applications.

## EXPERIMENTAL

### Materials

All reagents were purchased from Aldrich, Acros, or Strem Chemicals and were used as received. CuI used for films was purified using a literature procedure.<sup>52</sup>

### Instrumentation

#### **Single Crystal X-ray Diffraction**

Crystals were mounted on glass fibers and analyzed at 100 K, except where noted differently. All measurements were made using graphite-monochromated Cu K $\alpha$  radiation on a Bruker-AXS three-circle diffractometer, equipped with a SMART Apex II CCD detector.<sup>53</sup> Initial space group determination was based on a matrix consisting of 120 frames. The data were reduced using SAINT+,<sup>54</sup> and empirical absorption correction applied using SADABS.<sup>55</sup>

Structures were solved using SIR-92<sup>56</sup> or SHELX.<sup>57</sup> Least-squares refinement was carried out for all structures on  $F^2$  using SHELX-13 and ShelXle.<sup>58</sup> The non-hydrogen atoms were refined anisotropically. In all cases, hydrogen atoms were located the Fourier difference map and then placed in theoretical positions.

### **Powder X-ray Diffraction (PXRD)**

Powder X-ray diffraction (PXRD) data for **1**, **2**, **3a**, and **3b** were collected at George Washington Univ. using Rigaku Miniflex diffractometer with Cu K $\alpha$  radiation. For compound **3b** a 10 h scan was necessary due to weak response. In this case, the compound was milled with Paratone N oil to prevent its conversion to **3a**. Scans were carried out from 3 to 60° 2 theta at 2 deg./min. The data were processed using the MDI-Jade 6.1 software package.<sup>59</sup>

Powder X-ray diffraction (PXRD) data for **4** and **5** were collected using Bruker instrument described above as mulls using Paratone N oil. Cul films were also analyzed using this instrument. The films were adhered onto the X-ray sample mount with double sided tape. Three 180 s frames were collected, covering 5–60° 2 $\theta$ . Frames were merged using the SMART Apex II software<sup>53</sup> and were further processed using DIFFRAC-Plus and EVA software.<sup>60</sup> All calculated powder patterns from single crystal structural data were produced using Mercury software.<sup>61</sup>

### **Thermogravimetric Analysis (TGA)**

Thermogravimetric analyses (TGA) were conducted using a TA Instruments Q500 in the dynamic (variable temp.) mode with a maximum heating rate of 50 °C/min to 800 °C under 60 mL/min N<sub>2</sub> flow.

### **Differential Scanning Calorimetry (DSC)**

Differential scanning calorimetry (DSC) was conducted using a TA Instruments Q20 in the ramp mode with a scanning rate of 3 °C/min from 0 to 50 °C.

### **Chemical Analysis**

Analysis for C and H were carried out by Atlantic Microlabs, Norcross, GA.

### **Optical Microscopy**

Optical microscopy was carried out using an Olympus 1X71 inverted optical microscope capable of electronically viewing and capturing images. Film thickness estimates of the CuI films were also obtained using a calibrated z-stage. By noting the position of the z-stage when focusing on the glass cover slip and when focusing on the film surface, an approximate film thickness was determined.

### **Atomic Force Microscopy (AFM)**

Atomic Force Microscopy (AFM) images were obtained using an Ntegra Prima Atomic Force Microscope (NT-MDT) used in semi-contact mode with an ACTA probe (AppNano, 40 N/m nominal spring constant).

### **Scanning Electron Microscopy with Energy Dispersive Spectroscopy (SEM/EDS)**

SEM/EDS was performed on a Hitachi S-3400N scanning electron microscope equipped with a Bruker Quantax model 400 energy dispersive



spectrometer using an XFlash® 5010 EDS detector with a 129 eV resolution. Samples were mounted on double-sided carbon tape affixed to an aluminum specimen holder. Images were taken at a working distance of 10 mm with an accelerating voltage of 15 kV. EDS spectra were also collected under the same conditions for 2 min live time.

### **Raman Spectroscopy**

Raman spectroscopy measurements were performed on an inverted microscope. An excitation wavelength at 632.8 nm from a HeNe laser (Research Electro-Optics, LHRP-1701) was filtered (Semrock, LL01-633-25) and focused to the sample using a 20× objective (Nikon CFI, NA = 0.5). Scattering from the sample was collected through the objective, filtered (Semrock, LP02-633RS-25), focused to the entrance slit of the spectrograph (Princeton Instruments, SP2356), and dispersed using a 600 g/mm grating blazed at 500 nm. The observed Raman frequencies were calibrated using a cyclohexane standard. The excitation power ( $P_{exc}$ ) and acquisition time ( $t_{aq}$ ) were varied in order to maximize signal-to-noise ratios while avoiding molecular photobleaching.

Raman spectroscopy of neat pyridine, solid CuI, and solid  $Cu_4I_4Py_4$  was performed using the Delta Nu Advantage Series 785 bench-top Raman spectrophotometer. The excitation wavelength was 785 nm and calibration was done using polystyrene.

## Luminescence Spectroscopy

Measurements were carried out at the Univ. of Maine. Steady-state photoluminescence spectra were recorded with a QuantaMaster-1046 photoluminescence spectrophotometer from Photon Technology International. The instrument is equipped with two excitation monochromators and a single emission monochromator with a 75 W xenon lamp. Low temperature steady-state photoluminescence measurements were achieved by using a Janis St-100 optical cryostat equipped with a Honeywell temperature controller. Liquid nitrogen was used as coolant. Spectra were collected as sequential emission scans to form a 3-D matrix with excitation as the x axis, emission on the y axis, and intensity on the z axis. The wavelength of the exciting light was run from high to low wavelength at increments of 3 nm between 500 and 200 nm to avoid photobleaching, oxidation or other forms of degradation.

For lifetime measurements at 293 K and 77 K, excitation was provided by an Opolette™ (HE) 355 II UV tunable laser operating at 335 nm. The 335 nm excitation was chosen since all samples could be excited at this wavelength. The laser has a Nd:YAG flashlamp pumped with a pulse repetition rate of 20 Hz and an average output power 0.3 mW. The detection system is composed of a monochromator and photomultiplier from a JobinYvon Ramanor 2000M Raman spectrometer. Data were collected by a Le Croy 9310C dual 400 MHz oscilloscope collecting data every 10 ns for 50  $\mu$ s per sweep averaging 1000 sweeps per sample. Each sample was run 3 times through this 1000 sweep cycle and the results were averaged. The decay curves from these measurements

were fitted using an exponential decay fitting method in Origin Pro 8. The lifetimes were observed at the ideal emission wavelengths for compounds as determined by luminescence spectroscopy.

### **Static Partial Pressure-Dependent Fluorimetric Analysis System**

Our in-house-built fiber-optic fluorimeter (Figure 11) utilizes a bundle consisting of six optical fibers around one. The six outer fibers carry 365 nm excitation light from an LED source, and the center fiber carries emission light to the detector (Figure 12). Data were processed with SpectraSuite software (Ocean Optics, Dunedin).

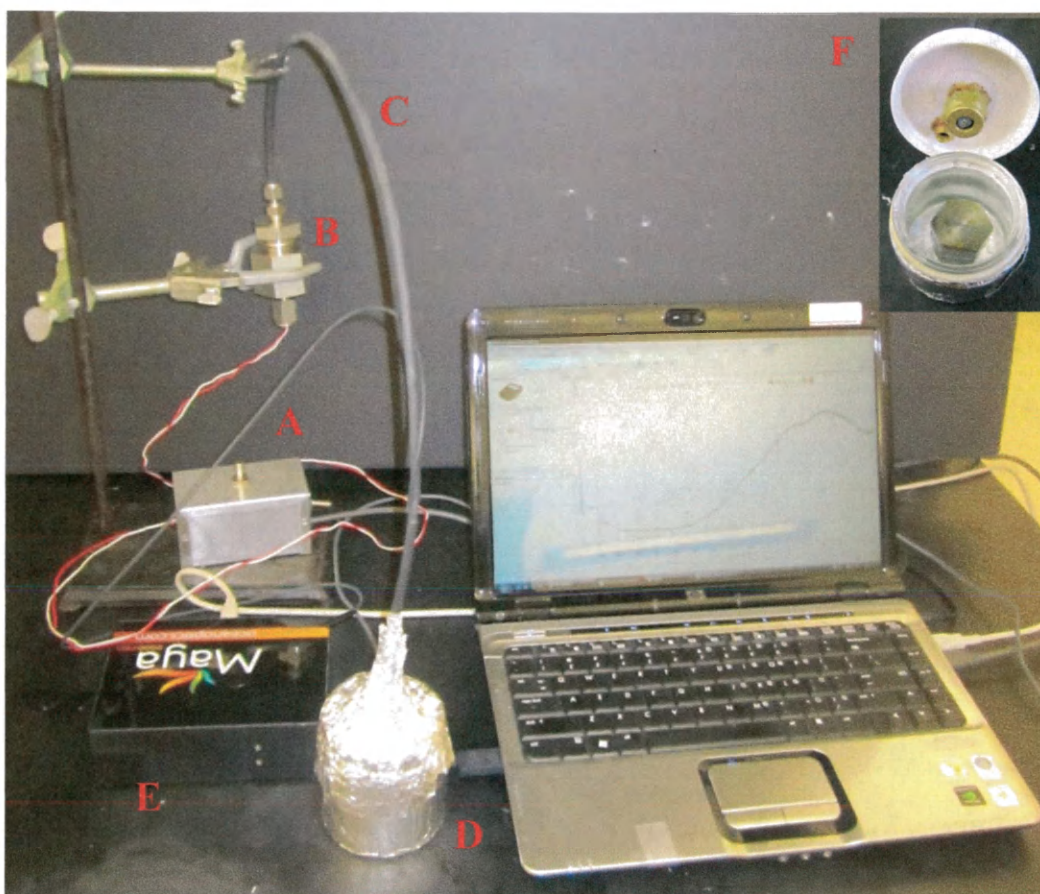


Figure 11. Spectrofluorimeter for measurement of inorganic substrate/VOC emission response. (A) LED controller, (B) LED source and filter enclosure, (C) fiber optic bundle, (D) sample chamber, (E) detector; inset: (F) inside view of sample chamber

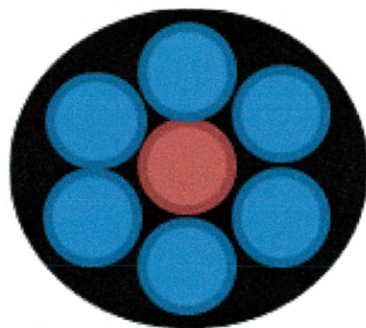


Figure 12. Schematic of fiber optic bundle consisting of six outer fibers carrying 365 nm excitation light (blue circles) and one inner fiber carrying emission to the detector (red circle).

Films were placed inside the sample chamber either pre-exposed or unexposed, depending on the experiment. The sample chamber contains an injection port so that unexposed films could be exposed to a set concentration of VOC, in this static system, and monitored using the spectrofluorimeter.

### **Flowing Partial Pressure-Dependent Fluorimetric Analysis System**

The schematic for the flowing analysis system is shown in Figure 13. This system utilized the fiber optic bundle described above (Figure 12). A syringe pump provides a supply of VOC. Less than 1 mL of neat VOC was placed in the syringe. The headspace of the syringe provided a steady supply of analyte gas for the flowing system. The analyte gas was mixed with a carrier gas ( $N_2$ ) which continuously flows into the sample chamber. The gas then flows out of the sample chamber into the outlet tubes and into a vented fume hood.

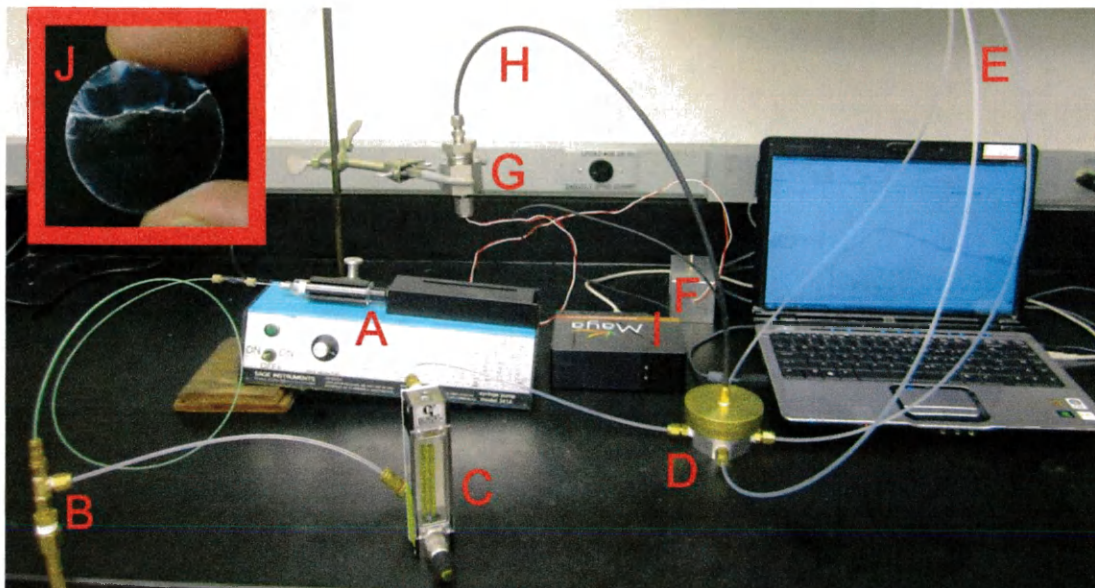


Figure 13. Spectrofluorimeter for measurement of inorganic substrate/VOC emission response in a flowing system. (A) Syringe pump, (B) mixing chamber for VOC and N<sub>2</sub> gas, (C) flow meter, (D) sample chamber, (E) outlet gas tubes, (F) LED controller, (G) LED source and filter enclosure, (H) fiber optic bundle, (I) detector, (J) CuI film.

## Synthesis

### **Film Casting**

All films were cast on microscopy cover glasses that were pre-cleaned by dipping in concentrated nitric acid, rinsing with deionized water, and drying with acetone. 35  $\mu$ L of a 100 mM CuI/MeCN solution were used for all film casting. Film casting was performed via evaporation with or without leveling by use of a doctor blade, or by spin coating. The evaporated films were cast by allowing the evaporation of the solution from the glass coverslip, leaving a uniform film. The doctor blade-leveled films were cast by running a doctor blade with a gap height

of 0.635 mm across the solution on the glass slide followed by the evaporation of the remaining solution. The evaporation of the MeCN occurred within 5 min for both methods.

### **Spin-Coat Cul Film Casting**

Spin-coat Cul films were produced using a Laurell Technologies Corporation Spin Coater Model WS-400BZ-6NPP/LITE (REV. MS) programmed in three stages and equipped with a N<sub>2</sub> purge. In the first stage the spin coater was brought up to speed and set to 500 rpm for 5 s. The sample was applied at 500 rpm over 5 s. Using a 100 µL FinnPipette F2 (Thermo Scientific), 100 µL of 100 mM Cul solution were added to a glass cover slip during the second stage by applying the solution directly onto the spinning glass cover slip. Drying was carried out at 3000 rpm for 30 s. This method was repeated until the required multi-layer Cul film was obtained.

### **Cul Film Exposures to Saturated VOCs**

Cul films were placed on an aluminum stand inside a 4 oz. glass jar (Figure 9). A few drops of VOC were added to the bottom of the jar, which was then sealed with a screw cap. The films were exposed for 10 min before being analyzed.



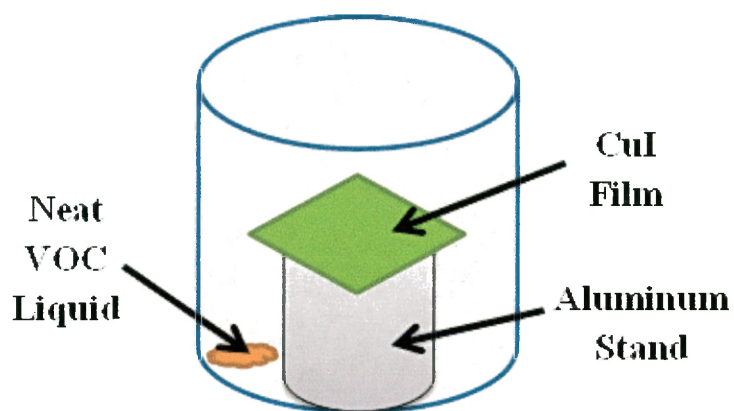


Figure 14. Vapor exposure chamber for CuI films.

### CuI-THT Product Synthesis

**(CuI)<sub>4</sub>(THT)<sub>2</sub>, 1.** 2.0 mL of 150 mM CuI in MeCN (0.30 mmol) and 2.0 mL of 250 mM THT in MeCN (0.50 mmol) were combined in a capped vial at 40 °C with stirring. A white precipitate with green luminescence formed immediately. The powder was collected by decanting, washed using ethyl ether, and vacuum dried (0.029 g, 0.031 mmol, 41%). Anal. Calcd. for C<sub>8</sub>H<sub>16</sub>Cu<sub>4</sub>I<sub>4</sub>S<sub>2</sub>: C, 10.24; H, 1.72. Found: C, 10.34; H, 1.66. TGA Calcd. for CuI: 81.2. Found: 81.6 (105–125 °C). Crystals of **1** were produced by layering 1.0 mL of 150 mM THT in MeCN (0.15 mmol) over 0.40 mL of 150 mM CuI in MeCN (0.060 mmol) in a capped vial at 40 °C and allowing diffusional mixing at 40 °C.

**(CuI)<sub>10</sub>(THT)<sub>7</sub>(MeCN), 2.** 2.8 mL of 150 mM CuI in MeCN (0.42 mmol) and 2.0 mL of 150 mM THT in MeCN (0.30 mmol) were combined in a capped vial at –10 °C with stirring. A white precipitate with yellow luminescence formed immediately. The powder was collected by decanting and immediately placing under vacuum for 2 h (0.065 g, 0.025 mmol, 60%). Anal. Calcd. for C<sub>30</sub>H<sub>59</sub>Cu<sub>10</sub>NI<sub>10</sub>S<sub>7</sub>: C, 14.06; H, 2.32. Found: C, 14.17; H, 2.23. TGA Calcd. for CuI: 74.3. Found: 74.5 (80–125 °C). Crystals of **2** were produced by layering 2.0



mL of 150 mM CuI in MeCN with 2.0 mL of 250 mM THT in MeCN and allowing diffusional mixing at room temp.

**(CuI)<sub>4</sub>(THT)<sub>4</sub>** (orange emission), **3a**. 2.0 mL of 150 mM CuI in MeCN (0.30 mmol) and 2.0 mL of 400 mM THT in MeCN (0.80 mmol) were combined in a capped vial at room temp. A white precipitate with orange luminescence formed immediately upon stirring. The powder was collected by decanting and immediately placing under vacuum for 2 h (0.035 g, 0.031 mmol, 42%). Anal. Calcd. for C<sub>16</sub>H<sub>32</sub>Cu<sub>4</sub>I<sub>4</sub>S<sub>4</sub>: C, 17.25; H, 2.87. Found: C, 17.12; H, 2.88. TGA Calcd. for (CuI)<sub>4</sub>(THT)<sub>2</sub>: 84.2. Found: 85.6 (90–100 °C). Calcd. for CuI: 68.4. Found: 70.6 (100–125 °C). Crystals of **3a** were produced by layering 2.0 mL of 150 mM CuI in MeCN with 2.0 mL of 250 mM THT in MeCN and allowing diffusional mixing at room temp.

**(CuI)<sub>4</sub>(THT)<sub>4</sub>** (dull yellow emission), **3b**. 1.5 mL of 150 mM CuI in MeCN (0.225 mmol) and 3.0 mL of 150 mM THT in MeCN (0.45 mmol) were combined in a capped vial at 0 °C. A white precipitate with dull yellow luminescence formed immediately upon stirring. The powder was collected by decanting and immediately placing on vacuum for 2 h (0.033 g, 0.030 mmol, 53%). Anal. Calcd. for C<sub>16</sub>H<sub>32</sub>Cu<sub>4</sub>I<sub>4</sub>S<sub>4</sub>: C, 17.25; H, 2.87. Found: C, 17.03; H, 2.79. TGA Calcd. for (CuI)<sub>4</sub>(THT)<sub>2</sub>: 84.2. Found: 84.5 (60–75 °C). Calcd. for CuI: 68.4. Found: 69.1 (75–115 °C). Crystals of **3b** were produced by layering 1.0 mL of 100 mM CuI in MeCN with 0.35 mL of neat THT and allowing diffusional mixing at 5 °C.

**(CuI)<sub>3</sub>(THT)<sub>3</sub>•MeCN**, **4**. 0.80 mL of 150 mM CuI in MeCN (0.12 mmol) and 2.0 mL of 150 mM THT in MeCN (0.30 mmol) were combined in a capped

vial at  $-5\text{ }^{\circ}\text{C}$  with stirring. A white precipitate with no luminescence formed immediately (0.012 g, 0.014 mmol, 34%). All attempts to isolate this product with drying caused traces of orange luminescence (indicative of **3a**) to develop immediately, rendering elemental analysis impossible. TGA Calcd. for  $(\text{CuI})_4(\text{THT})_4$ : 95.3. Found: 95.2 ( $40\text{--}55\text{ }^{\circ}\text{C}$ ). Calcd. for  $(\text{CuI})_4(\text{THT})_2$ : 80.2. Found: 79.7 ( $80\text{--}105\text{ }^{\circ}\text{C}$ ). Calcd. For CuI: 65.2. Found: 64.6 ( $125\text{--}140\text{ }^{\circ}\text{C}$ ). Crystals of **4** were produced by layering 2.0 mL of 150 mM CuI in MeCN with 5.0 mL of 150 mM THT in MeCN and allowing diffusional mixing at  $-8\text{ }^{\circ}\text{C}$ .

**$(\text{CuI})_2(\text{THT})_4$ , 5.** CuI (0.50 g, 2.6 mmol) was dissolved in 0.46 mL (5.3 mmol) neat THT in a capped vial at room temp. A white precipitate with no luminescence formed upon sonication. The powder was collected on a frit under vacuum (0.84 g, 1.1 mmol, 88%). All attempts to isolate this product with drying caused traces of orange luminescence (indicative of **3a**) to develop rapidly, rendering elemental analysis impossible. TGA Calcd. for  $(\text{CuI})_4(\text{THT})_4$ : 76.0. Found: 77.1 ( $45\text{--}75\text{ }^{\circ}\text{C}$ ). Calcd. For CuI: 51.9. Found: 52.7 ( $95\text{--}145\text{ }^{\circ}\text{C}$ ). Crystals of **5** were synthesized by producing a saturated solution of CuI in neat THT and storing at  $-8\text{ }^{\circ}\text{C}$ .

### **CuI-L Crystallizations**

#### **$(\text{CuI})_n(2\text{-Chloropyridine})_m$**

Crystals were produced by layering 1.0 mL of 0.53 M 2-chloropyridine in MeCN with 1.0 mL of 25 mM CuI in MeCN and allowing diffusional mixing at room temperature. The crystals produced were colorless needles with blue luminescence.

**(CuI)<sub>n</sub>(2-Bromopyridine)<sub>n</sub>**

Crystals were produced by layering 1.0 mL of 0.52 M 2-bromopyridine in MeCN with 1.0 mL of 25 mM CuI in MeCN and allowing diffusional mixing at room temperature. The crystals produced were colorless needles with blue luminescence.

## RESULTS AND DISCUSSION

### Cul Film Characterization

Characterization of the Cul films was performed in order to determine the optimal method to make the films for use as a VOC sensor. One desired film characteristic was a consistent and uniform surface. Several methods of film casting were attempted, including evaporation, doctor blade-casting, and spin coating. In the evaporation casting method, Cul solution was micropipetted onto a clean glass cover slip and allowed to evaporate. In the doctor blade method of casting, Cul solution was micropipetted onto a clean glass cover slip, the doctor blade was pulled over the solution, and the solution was allowed to evaporate. The doctor blade shown in Figure 15 was used. An image of a doctor blade film is also shown in Figure 15. The spin coating-cast Cul films were cast using a spin coater which spun the glass coverslip as the Cul solution was micropipetted onto it. The morphology of the resulting films was analyzed using optical microscopy, AFM, and SEM.

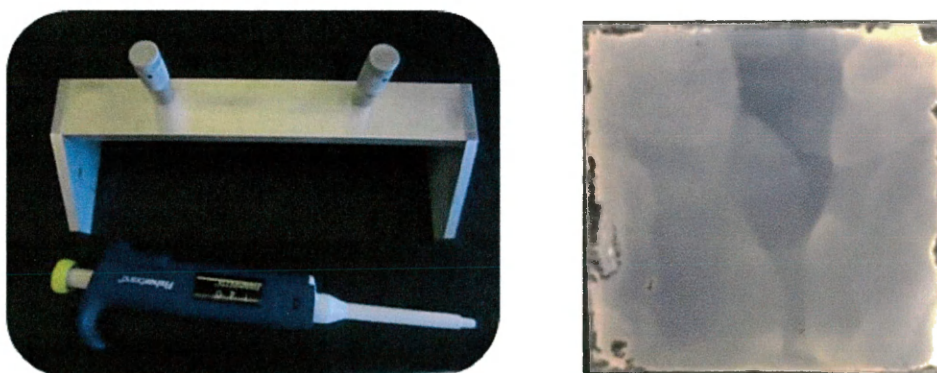


Figure 15. The doctor blade and micropipette used for film casting (left) and an image of a doctor blade cast Cul film (right).

The micrograph in Figure 16 shows the optical image of a doctor blade-cast Cul film. The Cul films are colorless; the optical microscopy images were rendered using false colors so that the morphology could be studied. The film was very consistent, with the exception of some black spots which were deemed to be holes in the film (Figure 16). These holes were apparently the result of dirt particles deposited from the air onto the glass substrate prior to film casting.

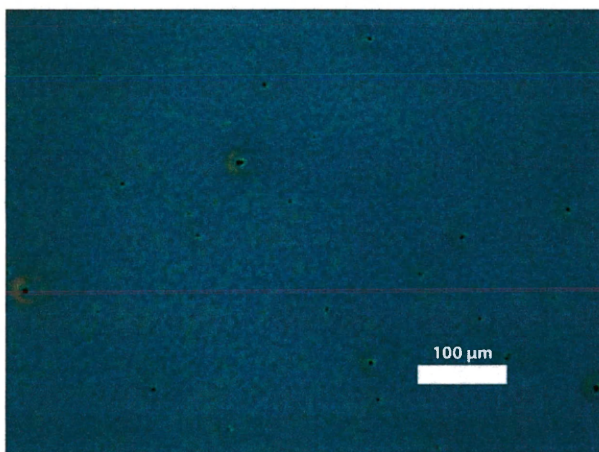


Figure 16. Optical micrograph of doctor blade-cast Cul film (rendered using false colors).

The Cul films cast by evaporation were not as physically uniform as the doctor blade-cast films. Figure 17 illustrates the films cast using the evaporation films casting method. The evaporation-cast films were not only rife with holes, but also contained many crystallites. These crystallites suggested that solution evaporation was sufficiently slow to allow crystallization. It was determined that evaporative casting is not the optimal technique for making Cul films due to the inconsistencies observed in optical microscopy.

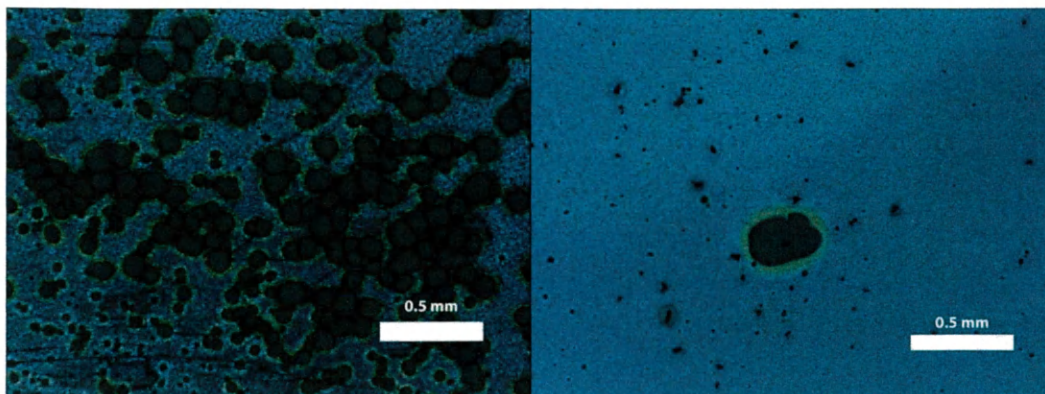


Figure 17. Optical micrographs of evaporation-cast CuI films (rendered using false colors).

Spin-coating was explored as an alternative method of film casting. Multiple spin-coated layers were attempted to optimize the process. The films displayed in Figure 18 were prepared with one coat and ten coats. The single coating on the first film was consistent in the center, but not toward the outside of the glass coverslip. The film with ten coatings was more consistent, but no more consistent than the doctor blade-cast films. The doctor blade-cast films were much more convenient to cast than the ten layered spin-coated films. So, doctor blade casting was retained as the optimal film casting method.



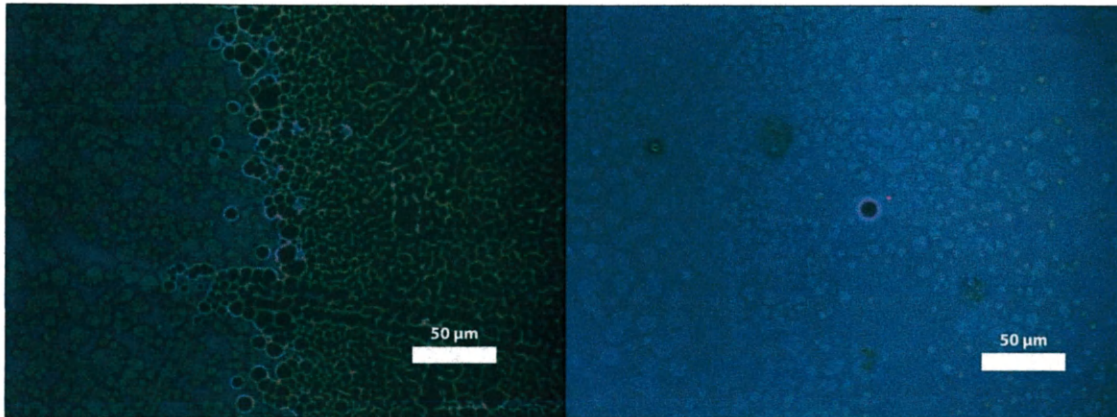


Figure 18. Optical micrographs of spin-coated CuI films, left: one coat, right: ten coats (rendered using false colors).

The morphology of the single-layer spin coat-cast CuI film was also investigated using AFM. This casting method produced the thinnest films, which allowed for analysis using this technique. It was hoped that these films would be sufficiently smooth to afford atomic resolution. The potential would then exist for looking at the film before and after exposure to VOC. Unfortunately, the film surface at the nanometer scale was found to be too rough to obtain atomic resolution (Figure 19).

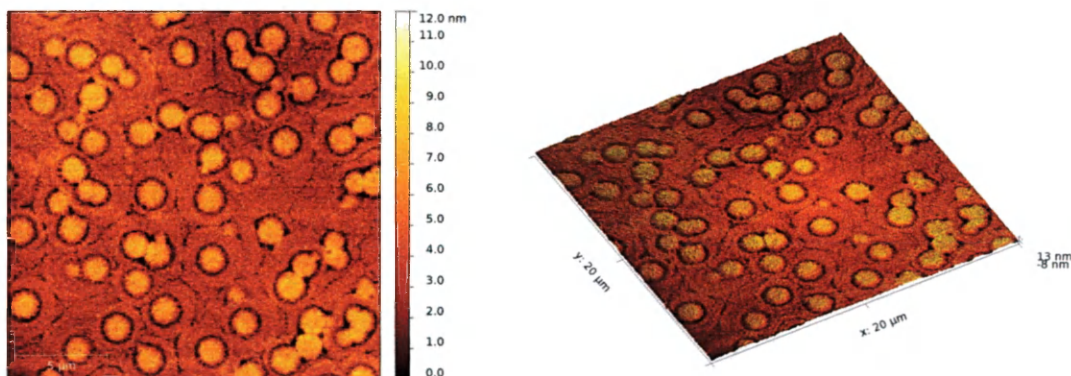


Figure 19. AFM micrographs of a single spin coated CuI film.

The film morphology of the doctor blade-cast films was further examined by other techniques because it was the most consistent and easy-to-cast film. SEM was used to probe the morphology of the CuI films. The EDS attachment to the SEM was also used to determine the consistency of the elemental distribution on the film. Figure 20 shows the SEM micrograph, as well as the EDS copper and iodine hypermaps. The SEM image further supports the consistency of the CuI films cast using the doctor blade. There is one abnormality in the center of this image, but a majority of the film surface was uniform. The EDS hypermaps represent elemental analysis maps of the film wherein copper is displayed in orange and iodide is displayed in blue. The SEM-EDS analysis indicated a uniform distribution of copper and iodine on the film.

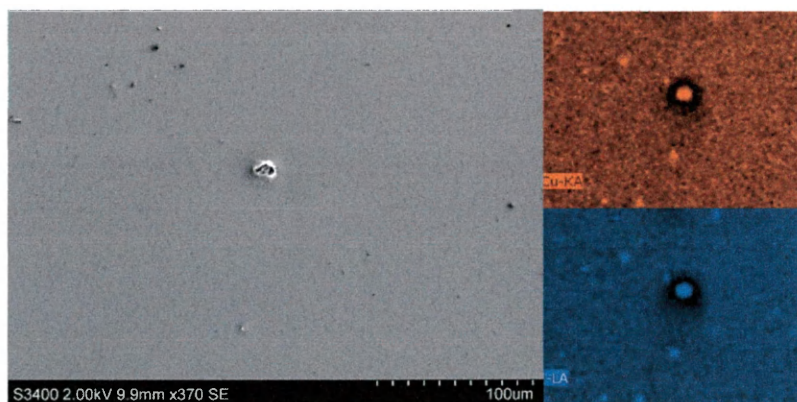


Figure 20. SEM micrograph of doctor blade cast CuI films with Cu and I EDS hypermaps (upper right and lower right, respectively).

Raman spectroscopy was employed to better understand adducts formed on the CuI surface after exposure to VOCs. The CuI film was analyzed before and after exposure to saturated partial pressure of Py. It should be noted that



Raman scattering intensity is inherently very weak, and without a very concentrated sample, it is difficult to obtain any signal at all. The exposed film produced a very weak Raman signal. The Raman spectra in Figure 21 are of the Cul film before and after exposure. Prior to exposure, only bands attributable to room light are evident. An additional peak at  $1006\text{ cm}^{-1}$  appears after the Cul film is exposed to Py.

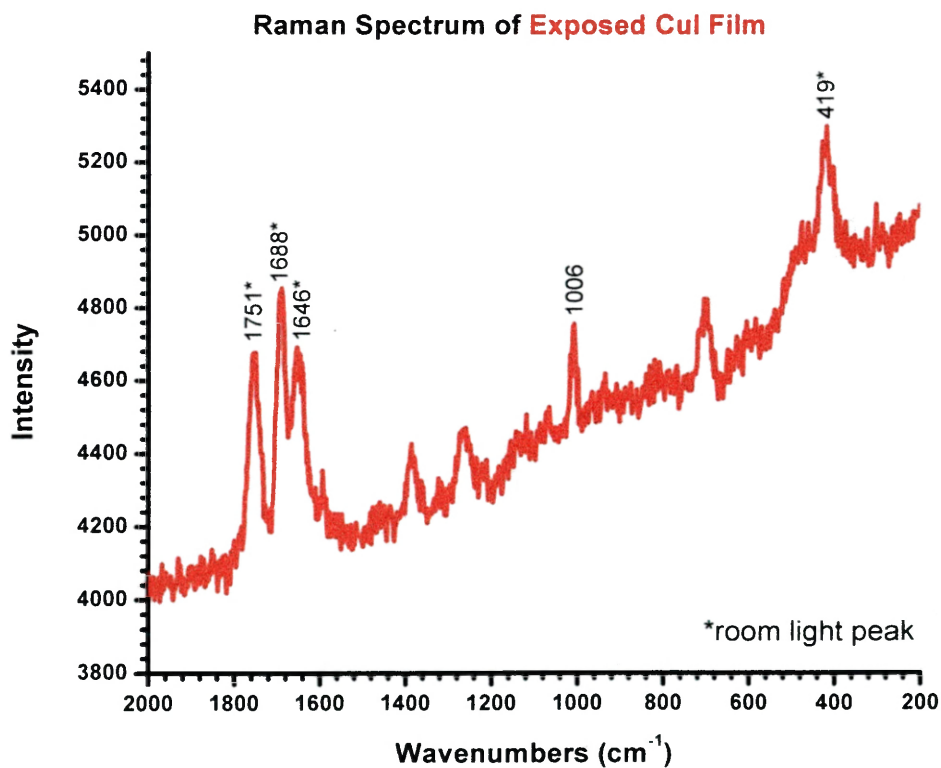
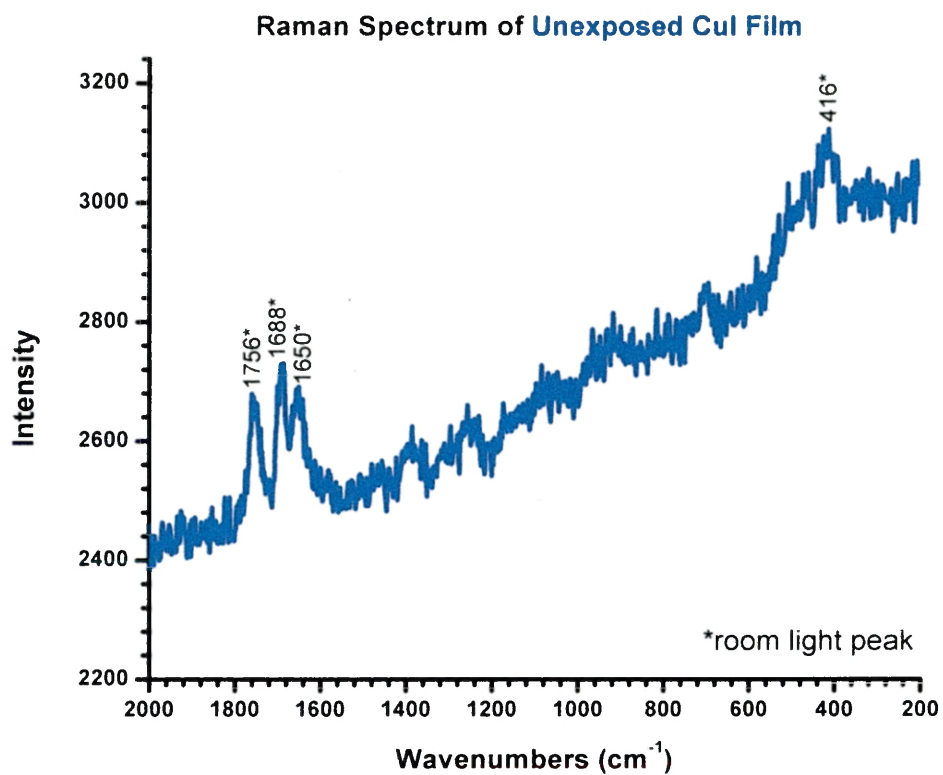


Figure 21. Raman spectrum of CuI films before (top) and after (bottom) Py vapor exposure.

Table 2. Raman results for unexposed and exposed CuI films, and for solid  $\text{Cu}_4\text{I}_4\text{Py}_4$  (room light peaks are excluded).

	<b>Bands (<math>\text{cm}^{-1}</math>)</b>			
<b>CuI film unexposed</b>	[none]			
<b>CuI film exposed</b>			1006	
<b><math>\text{Cu}_4\text{I}_4\text{Py}_4</math></b>	1602	1214	1010	629

In order to better understand these results, solid  $\text{Cu}_4\text{I}_4\text{Py}_4$  and CuI powder having been exposed to saturated partial pressure of Py were analyzed using a desktop Raman spectrometer. No difference was evident between the Py-exposed CuI powder and the complex of  $\text{Cu}_4\text{I}_4\text{Py}_4$ . The most striking peak match was for the most intense peak in Figure 22. The peaks appear at  $1006 \text{ cm}^{-1}$  and  $1010 \text{ cm}^{-1}$  for the solid  $\text{Cu}_4\text{I}_4\text{Py}_4$  and the CuI film exposed to Py, respectively (Table 2). The frequency represents the ring breathing vibrational mode ( $\nu_1$ ) in the  ${}^1\text{B}_2$  state of free pyridine.<sup>62-63</sup> Thus, the bonding of Py to the CuI film surface was successfully observed from the studies using Raman spectroscopy.

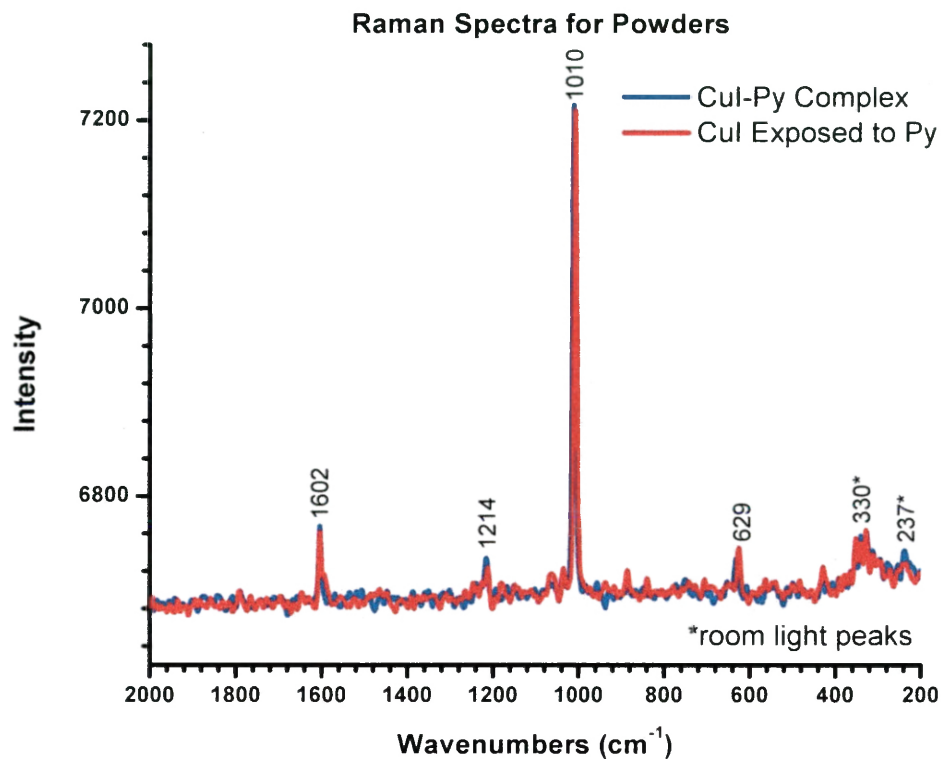


Figure 22. Desk-top Raman spectra of the  $\text{Cu}_4\text{I}_4\text{Py}_4$  and CuI solid exposed to Py.

The CuI films were further characterized using PXRD. The films were analyzed both before and after exposure to Py (Figure 23). Before exposure, the peaks were indexed which revealed the  $\gamma$ -CuI phase presence on the CuI films. A few additional peaks appear after exposure to saturated partial pressure of Py. These peaks are relatively weak in intensity presumably because they are due to a  $\text{Cu}_4\text{I}_4\text{Py}_4$  phase that is found only at the surface of the film. Thus, the  $\text{Cu}_4\text{I}_4\text{Py}_4$  surface adduct represents a new phase that is identifiable by PXRD

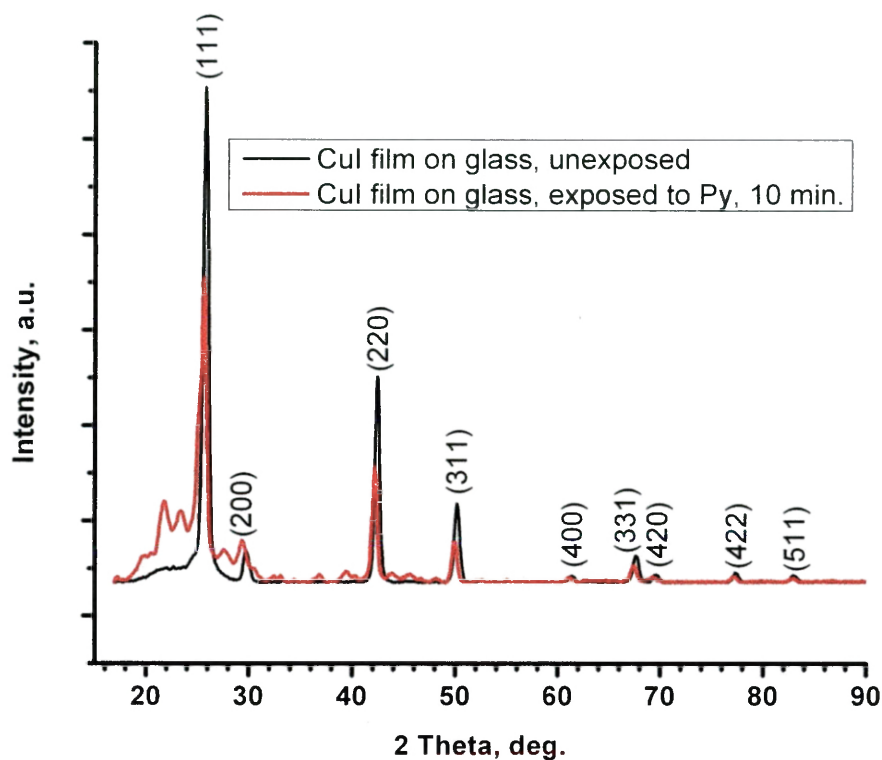


Figure 23. PXRD pattern of CuI film before and after exposure to saturated Py vapor.

TGA was another method used to characterize a single CuI film both before and after its exposure to saturated partial pressure of Py. Figure 24 shows the weight loss from the film irrespective of Py-exposure was less than 1.0%. Thus, the mass of the CuI film was found to be trivially small with respect to the mass of the glass coverslip. Moreover, any additional mass provided by adsorbed Py would lie far below levels detectable by TGA.

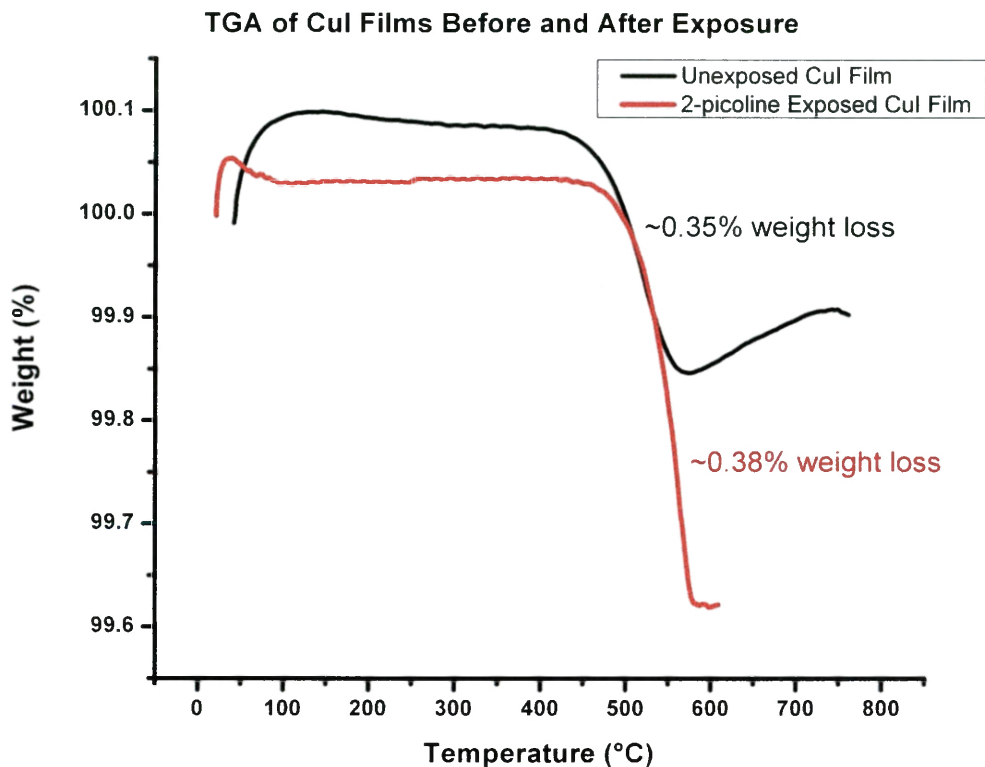


Figure 24. TGA traces for a Cul film before and after exposure to saturated Py vapor.

### Cul Film VOC Exposure Luminescence Results

#### **Saturated VOC Exposure**

Cul films were exposed to the saturated vapor pressure of various VOCs at ambient temperature. After the exposure, the luminescence of these films excited by 365 nm light was determined (Figure 25). A diverse variety of emission wavelengths were found, depending on the type of VOC used in the exposure. Unexposed Cul has an emission wavelength just within the visible region (~415 nm), which gave a purple color. The pyridine derivative VOCs are all blue-green emissive with the exception of 2-phenylpyridine and 4-

acetylpyridine (Figure 25 I–J). These VOC adducts emit in the orange-red region of the visible spectrum. The only other VOC adduct showing luminescence in the orange-red region was the CuI-THT adduct. The rest of the aliphatic amine and sulfide surface adducts had emission wavelengths in the blue, green, and yellow range.

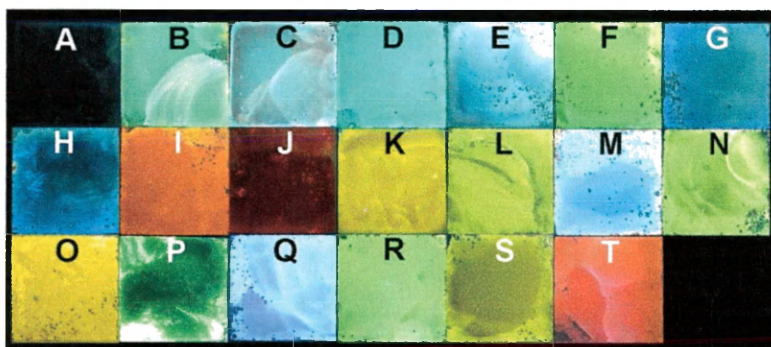


Figure 25. VOC exposed CuI films under 365 nm excitation light: (A) no exposure, (B) Py, (C) 2-Methylpyridine, (D) 3-Methylpyridine, (E) 4-Methylpyridine, (F) 2-Bromopyridine, (G) 3-Chloropyridine, (H) 3-Bromopyridine, (I) 2-Phenylpyridine, (J) 4-Acetylpyridine, (K) Piperidine, (L) N-Methylpiperidine, (M) N-Ethylpiperidine, (N) Morpholine, (O) N-Methylpyrrolidine, (P) N,N'-Dimethylpiperazine, (Q) N,N'-Diethylpiperazine, (R), Dimethylsulfide, (S) Diethylsulfide, (T) Tetrahydrothiophene (THT).

The emission wavelength for each of the VOCs in Figure 25 was determined using luminescence spectroscopy, wherein the excitation wavelength was varied to optimize emission response. The resulting emission wavelengths are shown in the spectra in Figures 26, 27, and 28. The aromatic amines lie within the range of 450 to 600 nm (Figure 26). The aliphatic amines have a wider

range from 400 to 650 nm (Figure 27). The sulfide amines lie between 500 and 600 nm (Figure 28).

A unique response was observed when the VOC tetrahydrothiophene (THT) was used. The exposure of CuI films to THT resulted in the formation of a various luminescent adducts on the same film. At room temperature, orange and green emission was observed. However, when the temperature was lowered to 77 K, yellow luminescence was observed. The presence of multiple phases of CuI-THT on the film surface led to further study of the CuI-THT system. The details of this study will be discussed below.

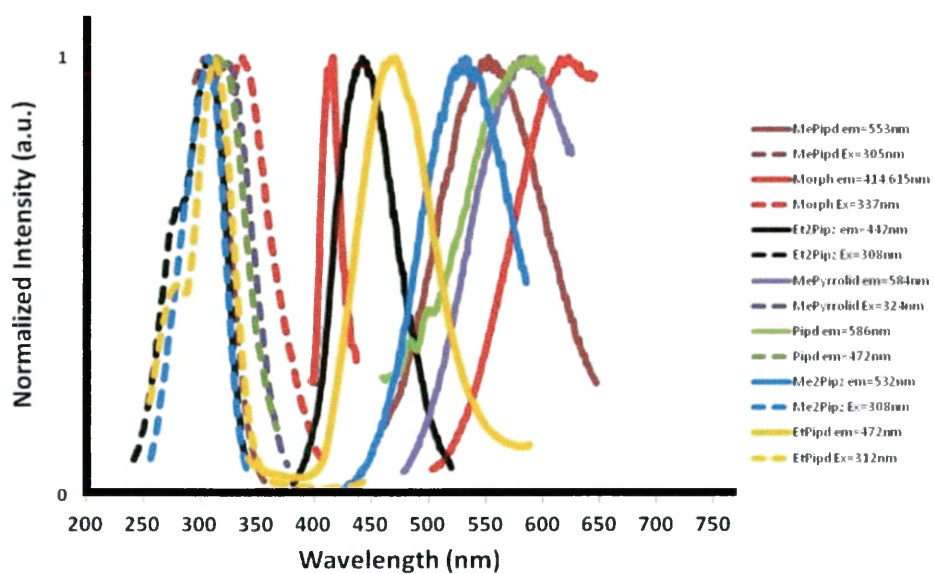


Figure 26. Ambient temperature luminescence spectra of CuI films after exposure to various VOCs. N-methylpiperidine (brown), morpholine (red), N,N'-diethylpiperazine (black), N-methylpyrrolidine (purple), piperidine (green), N,N'-dimethylpiperazine (blue), N-methylpiperidine (yellow)



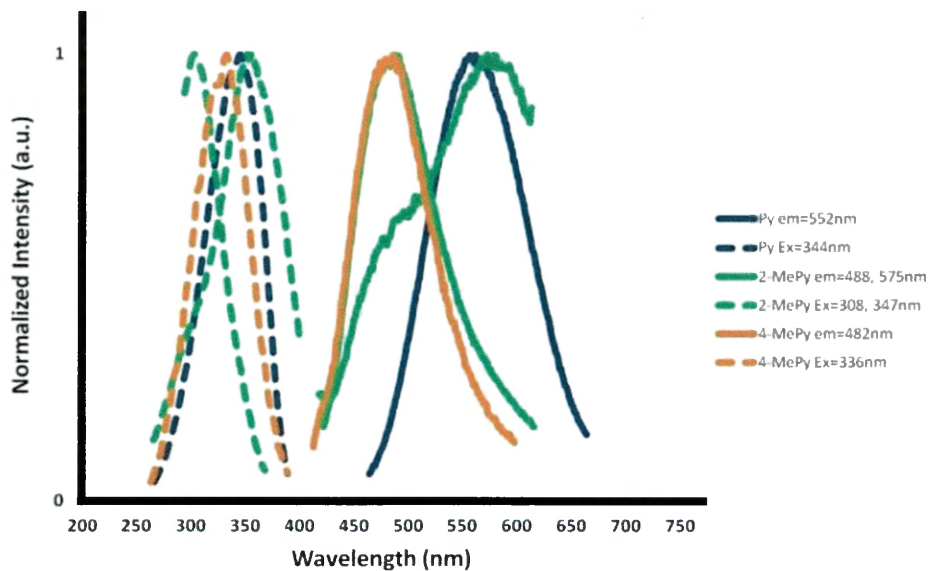


Figure 27. Ambient temperature luminescence spectra of CuI films after exposure to various VOCs. Pyridine (dark blue), 2-methylpyridine (green), 4-methylpyridine (orange)

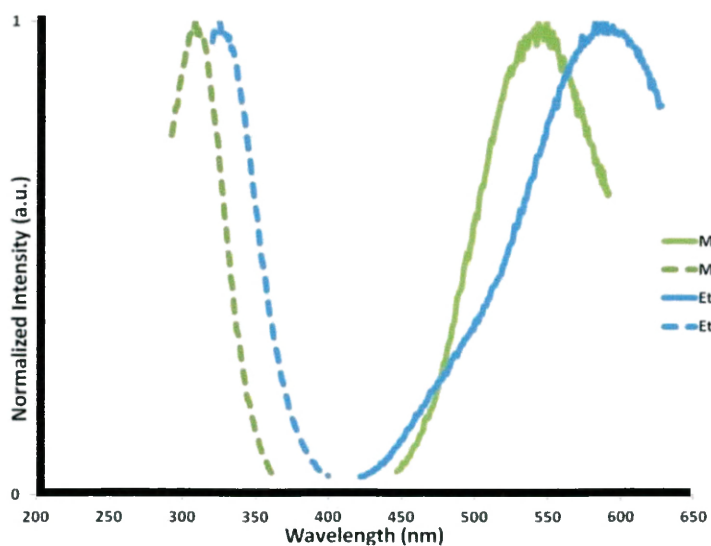


Figure 28. Ambient temperature luminescence spectra of CuI films after exposure to various VOCs. Dimethyl sulfide (light green), diethyl sulfide (light blue)

The diverse spectrum of luminescent colors observed from various VOCs suggested significant versatility for CuI as a sensor substrate. The CuI detector could use the compound-specific emission wavelengths observed to provide compound-specificity. The detector would also be a general sensor due to the ability of CuI to create adducts with amine and sulfide VOCs. Lastly, photoluminescence with a high quantum yield is sensitive and would make this detection design sensitive. The question remaining is whether or not the CuI detector can be used to detect VOCs at sufficiently low concentration to be useful.

### **Static Partial Pressure VOC Exposure**

Ambient temperature saturation vapor pressure produced observable emission for the CuI adducts with a variety of VOCs. In order to determine the limits of detection, an experiment was designed in which the saturation pressure of the VOC was halved as the starting point for a series of partial pressure experiments. The partial pressure would be lowered in subsequent tests if luminescence was observed at half saturation pressure. Two aromatic amines, 2-methylpyridine (2-MePy) and pyridine (Py), were thoroughly tested. The ambient temperature saturation partial pressures for 2-methylpyridine and Py are 10 Torr and 20 Torr, respectively.

Luminescence emission was observed as low as 4 Torr for the 2-methylpyridine vapor exposures, using luminescent spectroscopy (Figure 29). At lower partial pressures, some regions of each CuI film became emissive, but the

results were extremely inconsistent. It was therefore determined that the lowest partial pressure detectable for 2-MePy using CuI film is 4 Torr or 20.1 ppm. There is no established threshold level value for 2-MePy, so formaldehyde was used as a benchmark for a regulated VOC. Because the maximum permissible workplace level for the VOC, formaldehyde, mandated by OSHA is 0.75 ppm,<sup>1</sup> the CuI detector substrate does not appear to be sensitive enough for use in VOC detection.

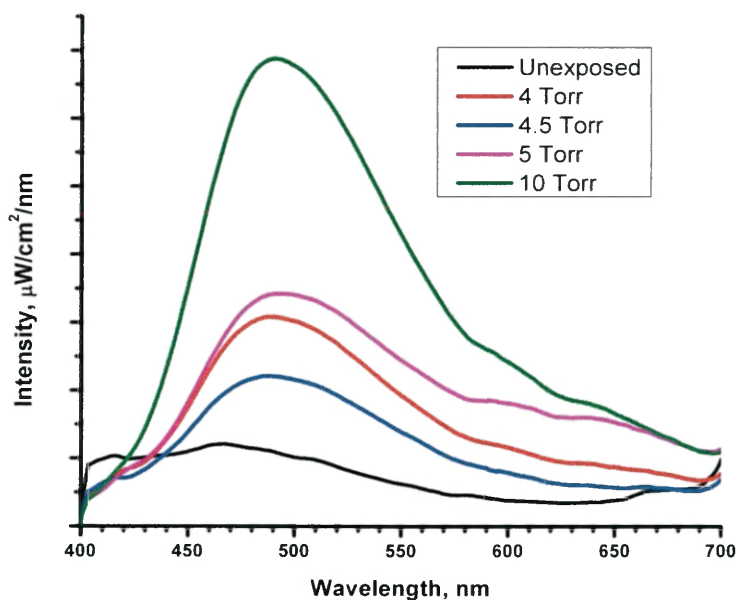


Figure 29. CuI film 15 min. 2-methylpyridine exposure using the static partial pressure-dependent fluorimetric analysis system at various partial pressures (saturation pressure of 2-methylpyridine is 10 Torr).

The CuI film adduct limit of detection was also tested using pyridine. The lowest detectable partial pressure of pyridine was found to be 5 Torr or 21.2 ppm (Figure 30). Again, this level of detection may not be sufficient enough to be an

effective sensor. However, before the CuI film could be eliminated as potential detector systems for trace level VOCs, another testing strategy was pursued.

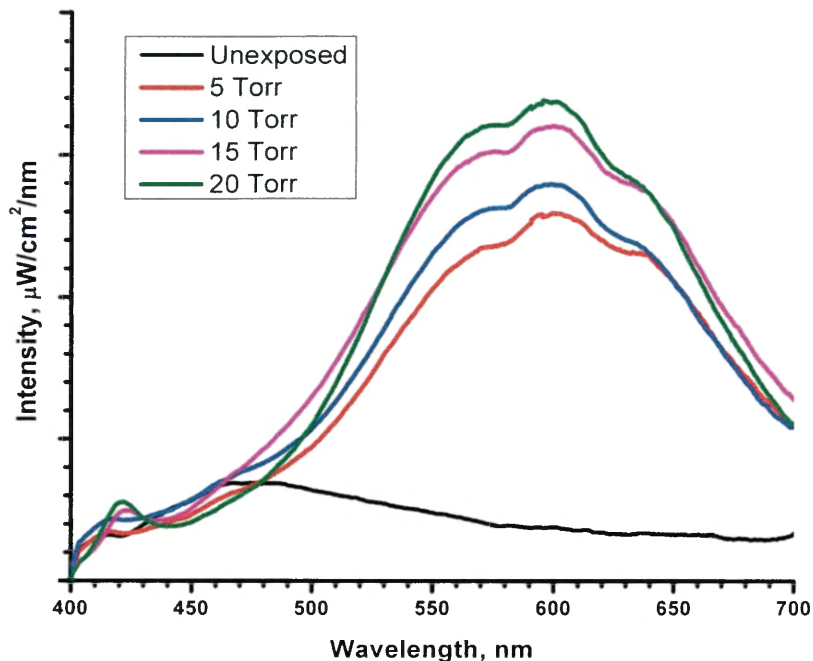


Figure 30. CuI film 15 min. pyridine exposure using the static partial pressure-dependent fluorimetric analysis system at various partial pressures (saturation pressure of pyridine is 20 Torr).

The flowing fluorimeter system was designed to ensure the CuI film was receiving a known concentration that would continuously flow over the film. The flow rate of the carrier gas and the flow rate of the analyte gas placed lower limitations on analyte gas flow. For this reason, this system was capable of providing a stream of pyridine at a maximum partial pressure of 2 Torr to the CuI film. No luminescence response on the CuI film was detected using the flowing system with pyridine at this pressure. After performing multiple tests on the CuI

films with the flowing fluorimeter system, it was determined that these films most likely cannot detect VOCs at low enough partial pressures to be effective.

### CuI-L Crystal Structures

CuI-halopyridine structures were of interest to us as part of our study of adducts made on the surface of the CuI film. Many CuI-halopyridine structures have as-yet unknown crystal structures. The two CuI-halopyridine structures in literature,  $(\text{CuI})_{\infty}(\text{3,5-diiodopyridine})_{\infty}$ <sup>64</sup> and  $(\text{CuI})_{\infty}(\text{5-bromopyridin-2-amine})_{\infty}$ <sup>65</sup> both have the stair step polymer crystal structure motif. In order to determine how common the stair step structures are for the CuI-halopyridine versus the cubane or dimer structure motifs, crystallization experiments were performed. As a result, two novel polymeric stair step crystal structures were solved:  $(\text{CuI})_{\infty}(\text{2-bromopyridine})_{\infty}$  and  $(\text{CuI})_{\infty}(\text{2-chloropyridine})_{\infty}$ . Refinement details for these crystal structures are summarized in Table 3 and selected bond lengths and angles are given in Table 4.

Table 3. Crystal and structure refinement data for  $(\text{CuI})_{\infty}(\text{2-bromopyridine})_{\infty}$  and  $(\text{CuI})_{\infty}(\text{2-chloropyridine})_{\infty}$ .

	<b><math>(\text{CuI})_{\infty}(\text{2-bromopyridine})_{\infty}</math></b>	<b><math>(\text{CuI})_{\infty}(\text{2-chloropyridine})_{\infty}</math></b>
<b>color and habit</b>	colorless needle	colorless needle
<b>size, mm</b>	0.29 x 0.04 x 0.04	0.36 x 0.11 x 0.05
<b>Formula</b>	$\text{C}_5\text{H}_4\text{BrCuIN}$	$\text{C}_5\text{H}_4\text{ClCuIN}$

<b>formula weight</b>	348.44	303.98
<b>space group</b>	$P2_12_12_1$	$P2_12_12_1$
<b>a, Å</b>	4.0956(2)	4.08230(10)
<b>b, Å</b>	11.5655(4)	11.4258(2)
<b>c, Å</b>	16.3272(6)	16.4107(3)
<b><math>\alpha</math>, deg</b>	90	90
<b><math>\beta</math>, deg</b>	90	90
<b><math>\gamma</math>, deg</b>	90	90
<b>volume, Å<sup>3</sup></b>	773.38(5)	765.45(3)
<b>Z</b>	4	4
<b><math>\rho_{\text{calc}}</math>, Mg m<sup>-3</sup></b>	2.993	2.638
<b>F<sub>000</sub></b>	632	560
<b><math>\mu(\text{Cu K}\alpha)</math>, mm<sup>-1</sup></b>	40.650	38.166
<b>temperature, K</b>	100	100
<b>residuals:<sup>a</sup> R; R<sub>w</sub></b>	0.0136; 0.0320	0.0216; 0.0545
<b>goodness of fit</b>	1.012	1.116
<b>Flack parameter</b>	0.753(6)	0.624(7)

Table 4. Selected bond lengths (Å) and angles (°) for  $(\text{CuI})_{\infty}(\text{2-bromopyridine})_{\infty}$  and  $(\text{CuI})_{\infty}(\text{2-chloropyridine})_{\infty}$ .

	$(\text{CuI})_{\infty}(\text{2-bromopyridine})_{\infty}$	$(\text{CuI})_{\infty}(\text{2-chloropyridine})_{\infty}$
<b>Cu-I</b>	2.6071(7) – 2.6881(8)	2.6071(7) – 2.6881(8)
<b>Cu-N</b>	2.060(4)	2.060(4)
<b>Cu<math>\cdots</math>Cu</b>	2.7348(8)	2.7348(8)
<b>I-Cu-I</b>	100.87(2) – 118.90(3)	100.87(2) – 118.90(3)
<b>I-Cu-N</b>	100.13(12) – 112.20(12)	100.13(12) – 112.20(12)

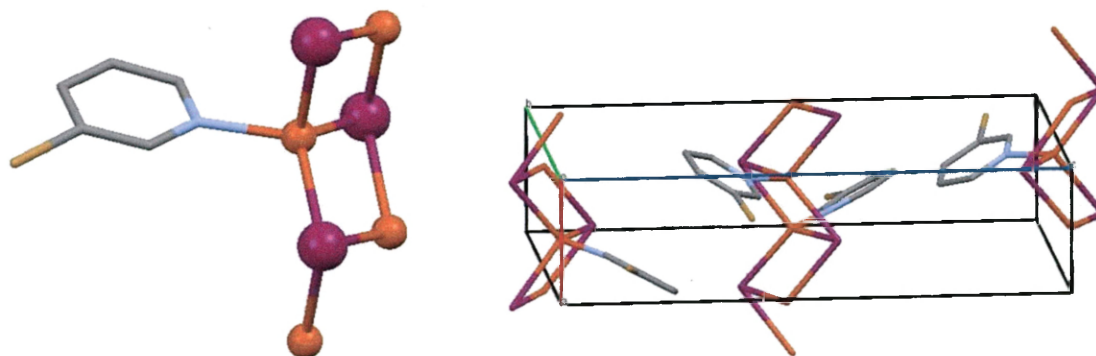


Figure 31.  $(\text{CuI})_{\infty}(\text{2-bromopyridine})_{\infty}$  polymeric stair step crystal structure (right), packing diagram (left). Key: Copper and iodine atoms shown as spheres. 2-bromopyridine shown as wireframe. Color scheme for X-ray figures: orange = Cu, purple = I, tan = Br, grey = carbon, blue = N. Hydrogen atoms omitted.

The crystal structure for  $(\text{CuI})_{\infty}(\text{2-bromopyridine})_{\infty}$  has a 1:1 stoichiometry, therefore, a ligand is attached at each copper site, as shown in Figure 31. The

compound  $(\text{CuI})_{\infty}(\text{2-bromopyridine})_{\infty}$  crystallizes in the non-centrosymmetric orthorhombic space group  $P2_12_12_1$ . The polymeric stair step crystal structure is essentially an open cubane or fused rhomboids that extends into an infinite chain. Tetrahedral geometry at the copper site is maintained. The same structural motif is observed in the previously discovered  $\text{CuI}$ -halopyridines,  $(\text{CuI})_{\infty}(\text{3,5-diiodopyridine})_{\infty}$ <sup>66</sup> and  $(\text{CuI})_{\infty}(\text{5-bromopyridin-2-amine})_{\infty}$ <sup>67</sup>. The  $\text{Cu-I}$  bond lengths (2.6071(7) – 2.6881(8) Å) are typical compared to the literature range which is from 2.498 – 3.423 Å. The  $\text{I-Cu-I}$  bond angles (100.87(2) – 118.90(3)°) are also within the typical range (85.08 – 126.371°).

The same crystal motif is observed for the  $(\text{CuI})_{\infty}(\text{2-chloropyridine})_{\infty}$  complex, which is isomorphic with the 2-bromopyridine analog described above.  $(\text{CuI})_{\infty}(\text{2-chloropyridine})_{\infty}$  also crystallizes in the space group  $P2_12_12_1$ . The structure is also a polymeric stair step, as seen in the known  $\text{CuI}$ -halopyridine structures, with tetrahedral geometry at the copper site (Figure 32). A ligand is attached to each copper site in this structure. The infinite stair step arrangement thus appears to be typical structural motifs for  $\text{CuI}$ -halopyridine complexes. The  $\text{Cu-I}$  bond lengths (2.6071(7) – 2.6881(8) Å) and  $\text{I-Cu-I}$  angles (100.87(2) – 118.90(3)°) lie within the ranges observed for  $\text{CuI}$  structures given above.  $\text{CuI}$ -THT complexes form a much more complex and diverse crystal system.



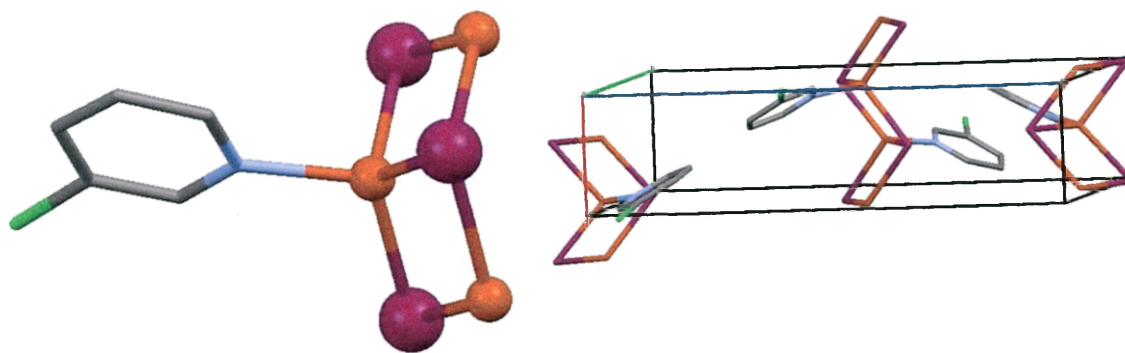


Figure 32.  $(\text{CuI})_{\infty}(\text{2-chloropyridine})_{\infty}$  polymeric stair step crystal structure (left) and packing diagram (right). Key: Copper and iodine atoms shown as spheres. 2-chloropyridine shown as wireframe. Color scheme for X-ray figures: orange = Cu, purple = I, green = Cl, grey = carbon, blue = N. Hydrogen atoms omitted.

### CuI-THT System

#### **Crystal Structures**

The unique behavior of CuI-THT on the film surface, as noted previously, led to a more extensive study of this system. Previously, only one structure from the CuI-THT system was known:  $(\text{CuI})_2(\text{THT})_4$ .<sup>25</sup> No photoluminescence data were reported on this compound, which proved to be non-emissive. Five novel structures, four of which are emissive, were discovered through an extensive study of the CuI-THT system.

Refinement details for these crystal structures are summarized in Table 5 and selected bond lengths and angles are given in Table 6. The first novel crystal structure,  $(\text{CuI})_4(\text{THT})_2$  (**1**) showed green luminescence under 365 nm irradiation. Complex **1** crystallized in the non-centrosymmetric orthorhombic space group

$P2_12_12_1$ . The repeat unit of **1** consists of a  $\text{Cu}_4\text{I}_4$  cubane with two THT ligands. The THT ligands bridge through single sulfur atoms forming a 3-D cubane network, as shown in Figure 34. The closed cubane units are linked to form puckered  $(\text{Cu}_4\text{I}_4)_6(\mu_2\text{-THT})_6$  rings. These rings come together at cubane nodes and are found in each of the three orthogonal directions. This type of bridging is rare having only been reported in  $[(\text{CuI})_4(\text{Me}_2\text{S})_3]$  and  $[(\text{CuI})_4(\text{Et}_2\text{S})_3]$  (Figure 33).<sup>33-36</sup> These structures differ from **1** due to their lack of true “closed” cubanes. Bridging through a single sulfur atom presumably caused crowding which is evident in some unusual compressed and open I–Cu–S bond angles, especially around Cu4 (range =  $93.64(12) - 117.00(13)^\circ$ ) (Figure 35). The cuprophilic Cu⋯Cu distances ( $2.636(3) - 2.759(3)\text{\AA}$ ) are slightly shorter than the van der Waals radius sum of  $2.8\text{\AA}$ . Otherwise, the bond lengths and angles in **1** are relatively unremarkable.

Table 5. Crystal and structure refinement data<sup>a</sup>

	<b>1</b>	<b>2</b>	<b>3<sup>a</sup></b>
<b>color and habit</b>	colorless block	colorless prism	colorless prism
<b>size, mm</b>	0.35 × 0.25 × 0.23	0.38 × 0.12 × 0.09	0.35 × 0.16 × 0.15
<b>Formula</b>	$\text{C}_8\text{H}_{16}\text{Cu}_4\text{I}_4\text{S}_2$	$\text{C}_{30}\text{H}_{59}\text{Cu}_{10}\text{I}_{10}\text{NS}_7$	$\text{C}_{16}\text{H}_{32}\text{Cu}_4\text{I}_4\text{S}_4$
<b>formula weight</b>	938.09	2562.60	1114.41
<b>space group</b>	$P2_12_12_1$ (#19)	$P2_1/m$ (#11)	$P2_1/n$ (#14)
<b>a, Å</b>	11.7527(2)	11.9107(4)	9.5824(2)
<b>b, Å</b>	11.8972(2)	12.2273(4)	34.9161(6)
<b>c, Å</b>	13.3762(2)	21.0371(6)	17.9841(3)
<b>α, deg</b>	90	90	90

<b><math>\beta</math>, deg</b>	90	97.434(2)	91.2810(10)
<b><math>\gamma</math>, deg</b>	90	90	90
<b>volume, <math>\text{\AA}^3</math></b>	1870.32(5)	3038.00(17)	6015.62(19)
<b>Z</b>	4	2	8
<b><math>\rho_{\text{calc}}</math>, <math>\text{Mg m}^{-3}</math></b>	3.331	2.801	2.461
<b><math>F_{000}</math></b>	1696	464	4160
<b><math>\mu(\text{Cu K}\alpha)</math>, <math>\text{mm}^{-1}</math></b>	58.888	46.043	38.037
<b>temperature, K</b>	100	123	250
<b>residuals:<sup>a</sup> R; <math>R_w</math></b>	0.0458; 0.1169	0.0545; 0.1531	0.0476; 0.1182
<b>goodness of fit</b>	1.080	1.140	1.064
<b>Flack parameter</b>	0.862(12)	–	–

<sup>a</sup> $R = R_1 = \sum ||F_o| - |F_c|| / \sum |F_o|$  for observed data only.  $R_w = wR_2 = \{ \sum [w(F_o^2 - F_c^2)^2] / \sum [w(F_o^2)^2] \}^{1/2}$  for all data.

Table 5 cont.

	<b>3b</b>	<b>4</b>
<b>color and habit</b>	colorless prism	colorless block
<b>size, mm</b>	0.31× 0.12× 0.09	0.47 × 0.29 × 0.19
<b>Formula</b>	$\text{C}_{16}\text{H}_{32}\text{Cu}_4\text{N}_4\text{S}_4$	$\text{C}_{14}\text{H}_{27}\text{Cu}_3\text{I}_3\text{NS}_3$
<b>formula weight</b>	1114.42	876.86
<b>space group</b>	$P-1$ (#2)	$C2/c$ (#15)
<b>a, <math>\text{\AA}</math></b>	9.5915(2)	22.7901(7)
<b>b, <math>\text{\AA}</math></b>	10.8378(3)	13.2617(4)
<b>c, <math>\text{\AA}</math></b>	15.7597(4)	16.0147(5)
<b><math>\alpha</math>, deg</b>	73.2170(10)	90
<b><math>\beta</math>, deg</b>	72.4319(12)	90.1331(11)
<b><math>\gamma</math>, deg</b>	69.2273(11)	90
<b>volume, <math>\text{\AA}^3</math></b>	1429.64(6)	4840.2(3)
<b>Z</b>	2	8

$\rho_{\text{calc}}$ , $\text{Mg m}^{-3}$	2.589	2.407
$F_{000}$	1040	3296
$\mu(\text{Cu K}\alpha)$ , $\text{mm}^{-1}$	40.013	35.514
temperature, K	100	100
residuals: <sup>a</sup> R; $R_w$	0.0501; 0.1621	0.0304; 0.0785
goodness of fit	1.163	1.175
Flack parameter	–	–

<sup>a</sup> $R = R_1 = \sum ||F_o| - |F_c|| / \sum |F_o|$  for observed data only.  $R_w = wR_2 = \{ \sum [w(F_o^2 - F_c^2)^2] / \sum [w(F_o^2)^2] \}^{1/2}$  for all data.

Table 6. Selected bond lengths (Å) and angles (°) for all CuI-THT complexes.

	1	2 <sup>b</sup>	3a
<b>Cu–I</b>	2.610(2)–2.756(3)	2.6098(14)–2.703(15)	2.6469(16)–2.709(3)
<b>Cu–S</b>	2.312(4), 2.317(4), 2.325(4)	2.307(4)–2.361(6)	2.284(3)–2.380(7)
<b>Cu<sup>⋯</sup>Cu</b>	2.636(3)–2.759(3)	2.650(5)–2.754(3)	2.6728(19)–2.837(3)
<b>I–Cu–I</b>	107.31(8)–118.02(9)	110.77(7)–120.76(11)	108.06(8)–116.29(6)
<b>Cu–I–Cu</b>	58.07(7)–62.20(7)	58.61(7)–63.67(6), 92.70(8), 97.58(7)	59.55(4)–64.09(5)
<b>I–Cu–S</b>	93.64(12)–117.00(13)	98.04(9)–124.26(17)	87.44(17)–118.81(16)
<b>S–Cu–S</b>	–	98.96(17), 99.08(15), 105.39(19)	–
<b>Cu–S–Cu</b>	120.47(17), 124.08(18)	117.51(18)–123.27(13)	–

<sup>a</sup>Data from ref. 25. <sup>b</sup>Bonding to Cu9 (10% occupancy) omitted.

Table 6 cont.

	3b	4	5 <sup>a</sup>
<b>Cu-I</b>	2.650(3)–2.728(3)	2.5887(8)–2.6418(7)	2.637(1), 2.639(1)
<b>Cu-S</b>	2.292(4), 2.293(4), 2.302(4), 2.306(4)	2.3187(11)–2.3517(10)	2.318(2), 2.331(3)
<b>Cu··Cu</b>	2.639(3)–2.768(3)	2.9653(14), 2.9722(9)	2.675(2)
<b>I-Cu-I</b>	109.67(9)–118.22(9)	110.40(2), 110.79(3), 110.86(2)	119.08(4)
<b>Cu-I-Cu</b>	58.29(7)–62.30(7)	69.06(3), 69.27(2), 69.43(2)	60.92(4)
<b>I-Cu-S</b>	98.97(13)–114.32(13)	107.04(4)–113.51(4)	104.6(1), 104.7(1), 104.7(1), 109.6(1)
<b>S-Cu-S</b>	–	102.49(4), 104.10(4), 104.64(5)	114.5(1)
<b>Cu-S-Cu</b>	–	120.26(5), 121.40(5), 128.78(5)	–

<sup>a</sup>Data from ref. 25. <sup>b</sup>Bonding to Cu9 (10% occupancy) omitted.

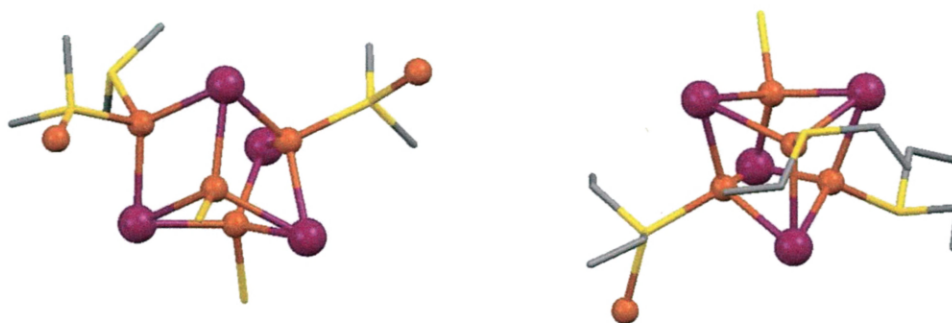


Figure 33. Crystal structures of  $(\text{CuI})_4(\text{Me}_2\text{S})_3$ <sup>34</sup> (left) and  $(\text{CuI})_4(\text{Et}_2\text{S})_3$ <sup>35</sup> (right).

Key: Copper and iodine atoms shown as spheres. THT are shown as wireframe.

Color scheme for X-ray figures: orange = Cu, purple = I, yellow = S, grey = carbon, blue = N. Hydrogen atoms omitted.

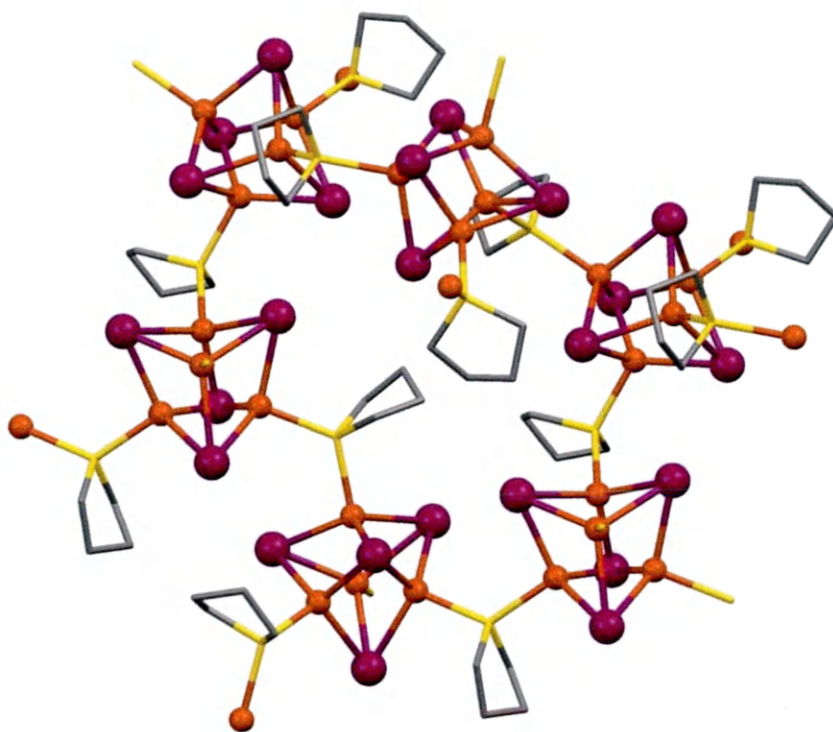


Figure 34. X-ray structure of  $(\text{CuI})_4(\text{THT})_2$ , **1**. Key: Copper and iodine atoms shown as spheres. THT are shown as wireframe. Color scheme for X-ray figures: orange = Cu, purple = I, yellow = S, grey = carbon, blue = N. Hydrogen atoms omitted.

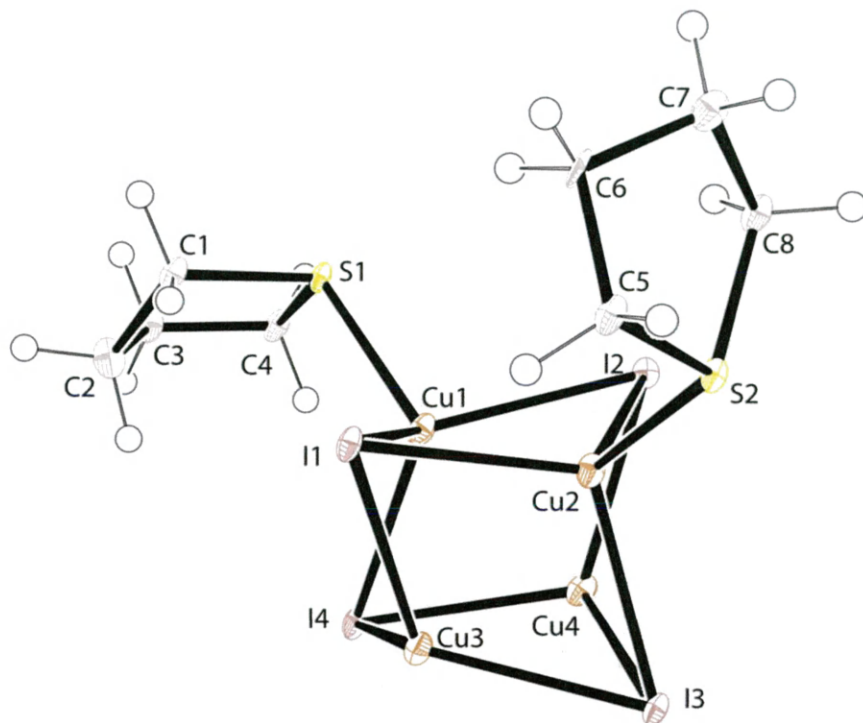


Figure 35. Thermal ellipsoid diagram for **1** (50% ellipsoids).

The complex and unprecedented X-ray structure of  $(\text{CuI})_{10}(\text{THT})_7(\text{MeCN})$  (**2**) (Figure 36) has a crystallographically independent unit that consists of eight unique Cu atoms, seven unique iodine atoms, and six unique THT ligands. This structure crystallizes in the centrosymmetric monoclinic  $P2_1/m$  space group. Disorder over two sites (Cu8 and Cu9) is present in the Cu atom bearing the MeCN ligand. There is significant disorder in three of the THT ligands which lie approximately on the crystallographic mirror plane. Two independent cubane units are present. An open cubane is formed by atoms Cu3, Cu4, Cu4' (prime indicates a mirror symmetry position), Cu5 and I2, I3, I4, I4'. The THT ligand on Cu5 is monodentate and Cu3 and Cu5 are bridged by  $\mu_2$ -THT ligands to a central rhomboid dimer  $\text{Cu}_2\text{I}_2$  (Cu1, Cu2, I1, and I1'). Therefore, Cu5 has a  $\text{I}_2\text{S}_2$

coordination sphere and Cu3, Cu4, and Cu4' each have an I<sub>3</sub>S coordination sphere. Two more μ<sub>2</sub>-THT ligands attach the other side of the rhomboid dimer to another cubane (Cu6, Cu7, Cu7', Cu8/9, I5, I6, I7, and I7'). When this cubane contains Cu8 (90% occupancy, see Figure 37), it is open. The cubane is "closed", however, when it contains Cu9 (10% occupancy, see Figure 37). The MeCN ligand on Cu8 acts as a monodentate capping ligand and is analogous to the S3 THT in that way. A long 1-D chain is formed from the structure described, (Cu<sub>4</sub>I<sub>4</sub>)-(μ<sub>2</sub>-THT)<sub>2</sub>-(Cu<sub>2</sub>I<sub>2</sub>)-(μ<sub>2</sub>-THT)<sub>2</sub>-(Cu<sub>4</sub>I<sub>4</sub>), and these chains knit together like rungs on a ladder by bridging μ<sub>2</sub>-THT ligands which link Cu4 and Cu7. The ladder rungs are in alternating directions. There is also a lack of crosslinking of the ladders, preventing the formation of 2-D sheets. All Cu...Cu distances in **2** are less than the van der Waals sum value. The Cu...Cu distances from the cubane Cu's to the swung out Cu (Cu3...Cu5 = 2.691(4), Cu6...Cu8 = 2.601(4) Å) do not significantly differ from those distances within the cubanes (Cu3...Cu4 = 2.700(3), Cu6...Cu7 = 2.680(3) Å). The Cu...Cu distance in the dimer (Cu1...Cu2) is somewhat longer (2.754(3) Å) while still lying in the van der Waals sum value. The Cu-I-Cu bond angles lie within the range of 58 – 63° with two exceptions due to the opening of the cubanes: Cu8-I7-Cu7' = 192.70(8) and Cu5-I4-Cu4' = 97.58(7) Å.



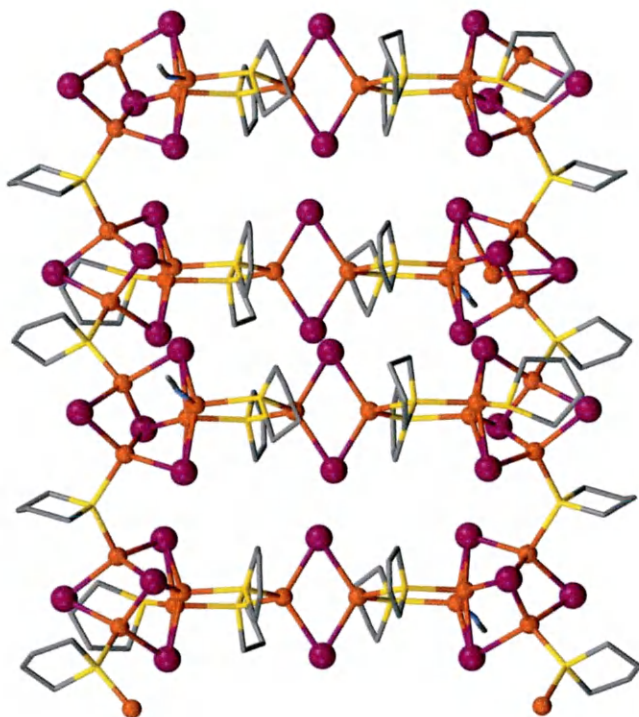


Figure 36. X-ray structure of  $(\text{CuI})_{10}(\text{THT})_7(\text{MeCN})$ , **2** with Cu8 (90% occupancy).

Key: Copper and iodine atoms shown as spheres. THT are shown as wireframe.

Color scheme for X-ray figures: orange = Cu, purple = I, yellow = S, grey = carbon, blue = N. Hydrogen atoms omitted.

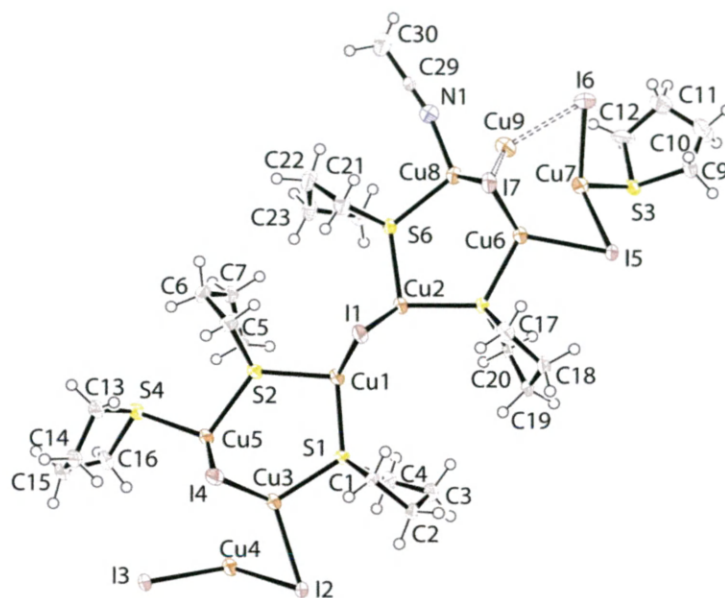


Figure 37. X-ray structure of **2** (50% ellipsoids). Cu8–NCMe present at 90% occupancy and Cu9 (dashed) present at 10% occupancy.

Complexes **3a** and **3b** are polymorphs, each having the simple cubane formula  $(\text{CuI})_4(\text{THT})_4$  (Figure 38). Compound **3a** crystallizes in the centrosymmetric monoclinic  $P2_1/n$  space group and has two crystallographically independent cubanes units in the unit cell. One of the THT ligands in this structure is disordered so that two ligand positions are bonded to Cu8 (Figure 39). The X-ray structure of **3a** was analyzed at 250 K due to a destructive phase change that occurred at 213 K, producing a triclinic cell. Compound **3b** crystallizes in the triclinic space group  $P\bar{1}$  with a single crystallographically independent cubane molecule. These polymorphs show different luminescence emission under 365 nm irradiation. Such different luminescent behavior in polymorphs was previously described for  $(\text{CuI})_4(\text{PPh}_3)_4$ .<sup>68</sup> Compound **3a** shows orange emission and compound **3b** has dull yellow emission. There are no meaningful differences amongst the bond lengths and angles of the three

cubanes, as demonstrated by overlaying the structures (Figure 40). For example, Cu–I distances in **3a** are 2.651(2) – 2.710(2) and 2.647(2) – 2.709(3) Å, and in **3b** are 2.650(3) – 2.728(3) Å; and Cu···Cu distances in **3a** are 2.673(2) – 2.761(2) and 2.669(2) – 2.837(3) Å, and in **3b** are 2.639(3) – 2.768(3) Å.

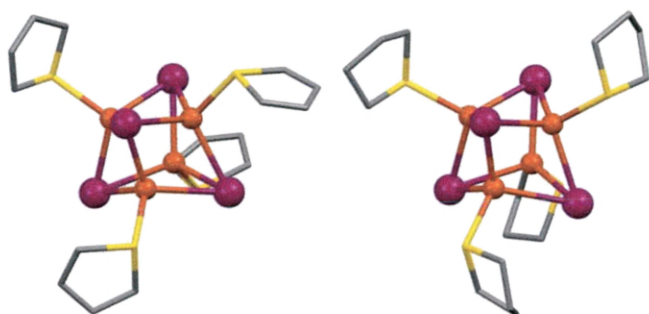


Figure 38. X-ray structures of  $(\text{CuI})_4(\text{THT})_4$  polymorphs **3a** (left) and **3b** (one molecule only shown, right). Key: Copper and iodine atoms shown as spheres. THT are shown as wireframe. Color scheme for X-ray figures: orange = Cu, purple = I, yellow = S, grey = carbon, blue = N. Hydrogen atoms omitted.

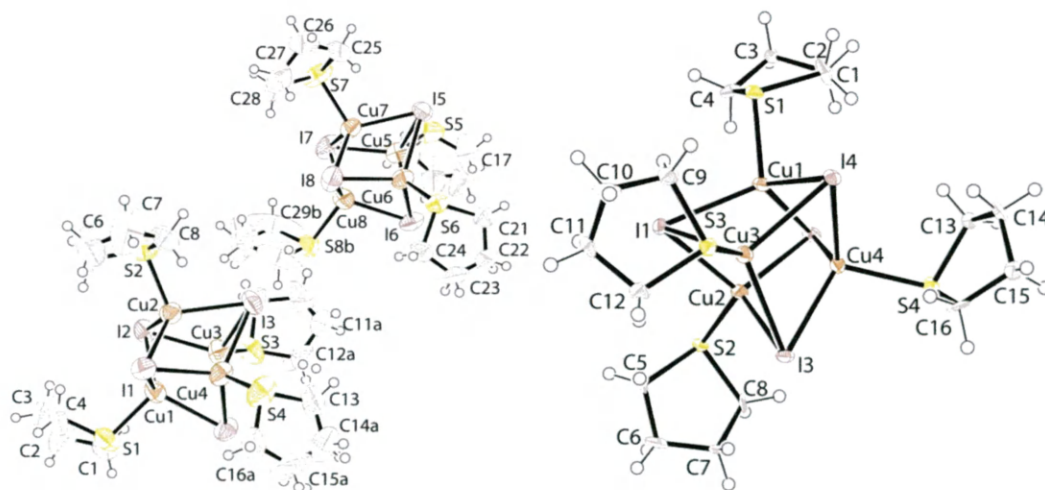


Figure 39. Thermal ellipsoid diagram of (a) **3a** and (b) **3b** (50% ellipsoids).

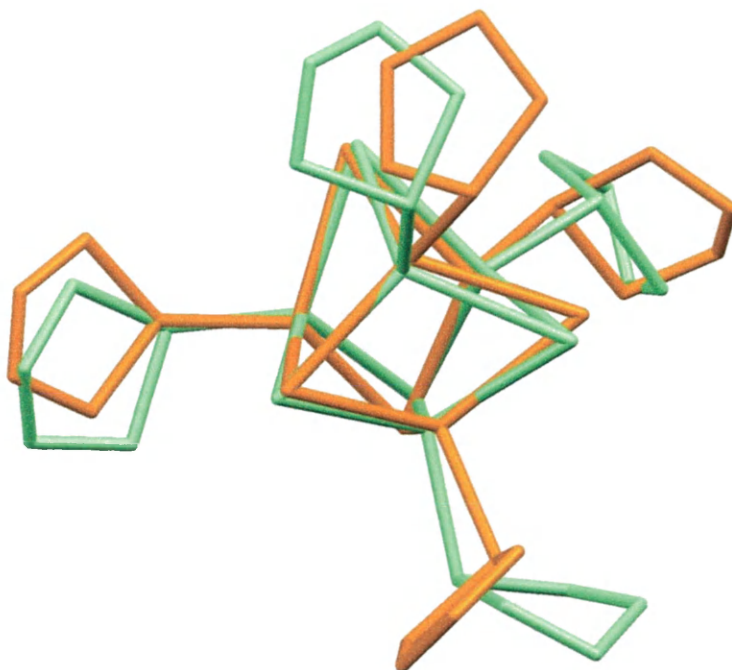


Figure 40. Wireframe overlay of **3a** (orange, one independent molecule only) and **3b** (green).

$(\text{CuI})_3(\text{THT})_3 \cdot \text{MeCN}$  (**4**) crystallizes in the centrosymmetric monoclinic  $C2/c$  space group and contains a non-coordinated MeCN molecule. It also shows bridging THT behavior leading to network formation, as seen in **1** and **2** (Figure 41 and Figure 42). Six-membered  $\text{Cu}_3\text{S}_3$  rings are formed by the linking of dimeric  $\text{Cu}_2\text{I}_2$  units through  $\mu_2$ -THT molecules. The six-membered rings are further overlaid into  $(\text{Cu}_2\text{I}_2)_6(\text{THT})_6$  macrocycles which form nearly flat 2-D sheets with the THT rings pointing towards the center of the larger rings. The distance between the sheets is rather small (interplanar  $\text{I} \cdots \text{I}$  distance = 4.3 Å). The solvent molecule, MeCN, is trapped between the sheets and aligned with the center of the large rings. In this compound, the  $\text{Cu} \cdots \text{Cu}$  interactions (2.9653(14), 2.9722(9))

Å) are longer than the van der Waals sum. This effect is further reflected in the relatively open Cu–I–Cu bond angles of  $69.06(3) - 69.43(2)^\circ$ .

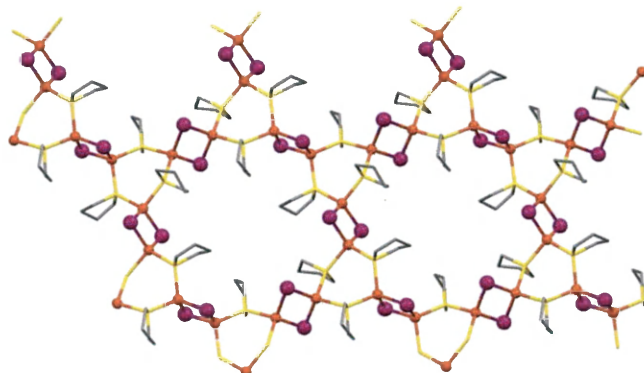


Figure 41. X-ray structure of  $(\text{CuI})_3(\text{THT})_3 \cdot \text{MeCN}$ , **4**. Key: Copper and iodine atoms shown as spheres. THT are shown as wireframe. Color scheme for X-ray figures: orange = Cu, purple = I, yellow = S, grey = carbon, blue = N. Hydrogen atoms omitted.

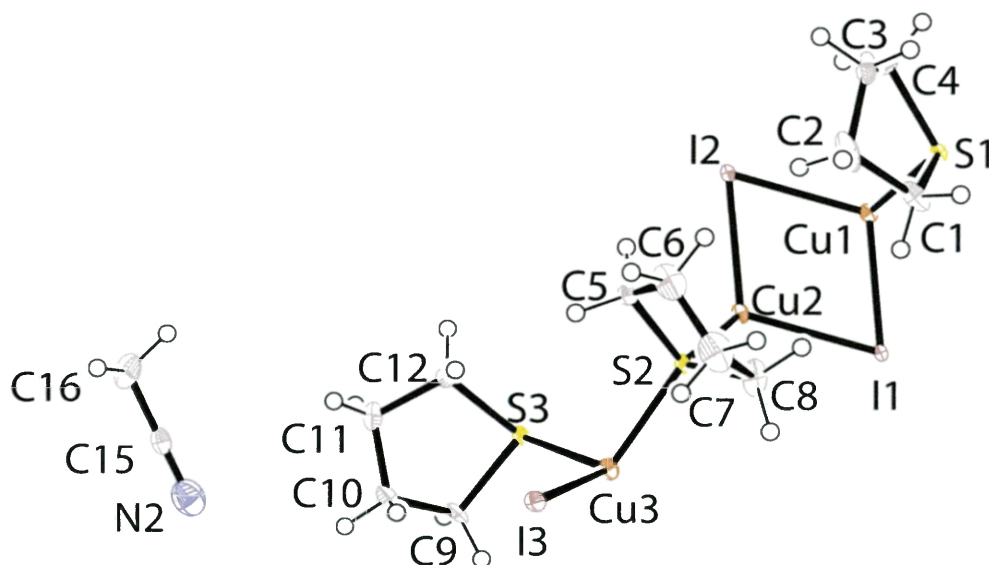


Figure 42. Thermal ellipsoid diagram of **4** (50% ellipsoids).

## CuI-THT Product Domain Diagram

Stirred crystallization experiments in capped vials containing various ratios of CuI and THT in MeCN at various temperatures were performed. All the experiments yielded white precipitates, with the exception of relatively CuI-rich mixtures at high temperatures, which failed to produce solids. The identity of the products from these stirred reactions was initially deduced from luminescence emission color observed. The solid products were later identified using PXRD and/or TGA. The resulting domain diagram in Figure 43 shows which CuI-THT phases are formed from MeCN at various temperatures and ratios of CuI:THT. At high temperatures and CuI-rich conditions, the green-emitting phase, **1**, was the result. At lower temperatures with the same CuI-rich conditions, the dull yellow-emitting compound **2** was produced. At around room temperature, but in THT-rich conditions, the orange-emitting **3a** phase was formed. If the temperature is lowered from the domain of **2**, the yellow-emitting phase, **3b** will be produced. At temperatures below 0 °C and in THT-rich conditions, the dark phase **4** was formed. The only one of the six CuI-THT products now known that was not observed in this study is the previously reported, and non-emissive dimer **5** (see Figure 8b).<sup>25</sup> Black light photos under 365 nm excitation for the four emissive phases **1**, **2**, **3a**, and **3b** are shown in Figure 44.



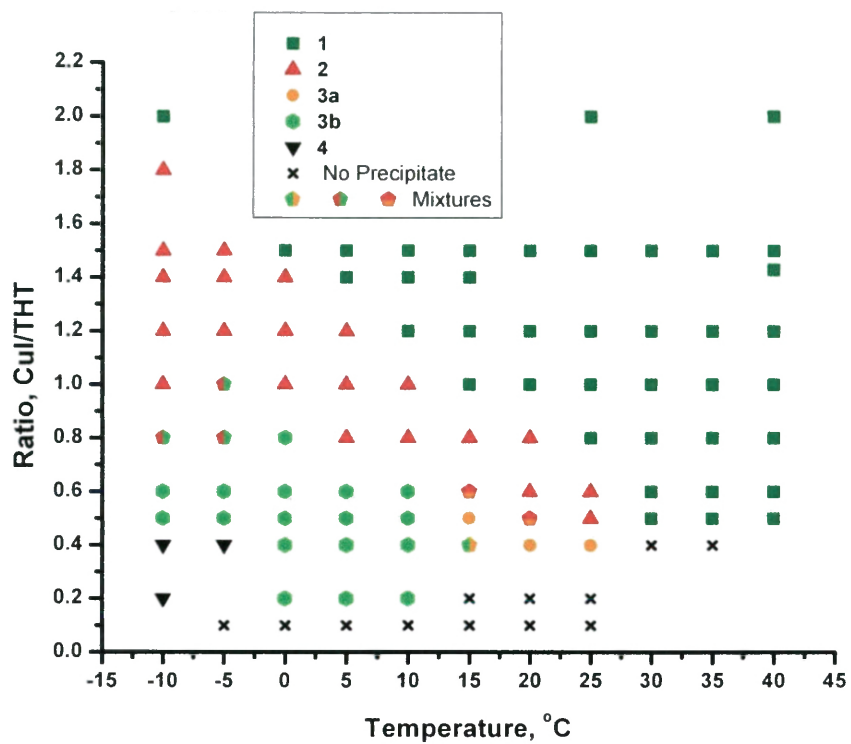


Figure 43. Precipitate domains for CuI-THT in MeCN at various mixing ratios and temperatures.

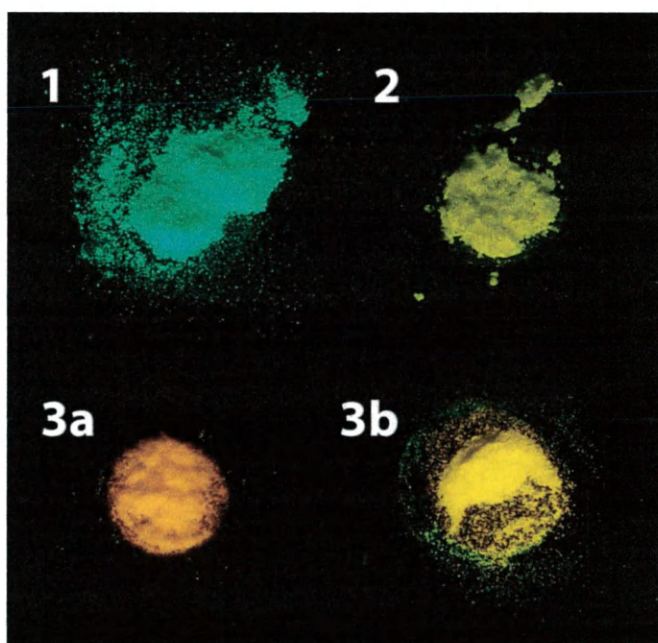


Figure 44. Photos of emissive phase CuI-THT powders under 365 nm excitation.

## PXRD of CuI-THT Powders

Samples of all six CuI-THT compounds were prepared using the optimal conditions as given in the domain diagram (Figure 43). Compound **5** was synthesized by a modification of the literature procedure in which solid CuI (rather than Cu/KI) was dissolved in neat THT.<sup>25</sup> These samples were then characterized using PXRD and the results compared to the calculated powder patterns from their respective crystal structures. Compounds **1**, **2**, **3a**, and **3b** were analyzed by PXRD at room temperature. Due to the loss of THT or solvent at ambient temperatures, **4** and **5** were analyzed at 100 K.

The PXRD pattern of **1** matches the calculated pattern extremely well (Figure 45). The PXRD pattern for **2** was more cluttered than the pattern for **1**, but still appears to match the calculated pattern well, as seen in Figure 46. Another strong match between the calculated and experimental PXRD patterns is observed for **3a** (Figure 47). Problems begin to arise with the PXRD patterns of **3b**, **4**, and **5**. Compound **3b** does not diffract very well, thus it required a long run to get measurable intensity (Figure 48). Preferred crystallite orientation is also a potential source problem because this compound could not be ground without losing THT and converting to **1** (grinding studies are discussed below). This could explain the intensities for the calculated pattern being different than the experimental pattern. The matches for **4** and **5** are good as seen in Figures 49 and 50, respectively, but each experimental trace possesses a peak that does not match the calculated pattern (each at around 22°). This peak could be the



result of sample contamination or the appearance of another phase due to solvent or THT loss.

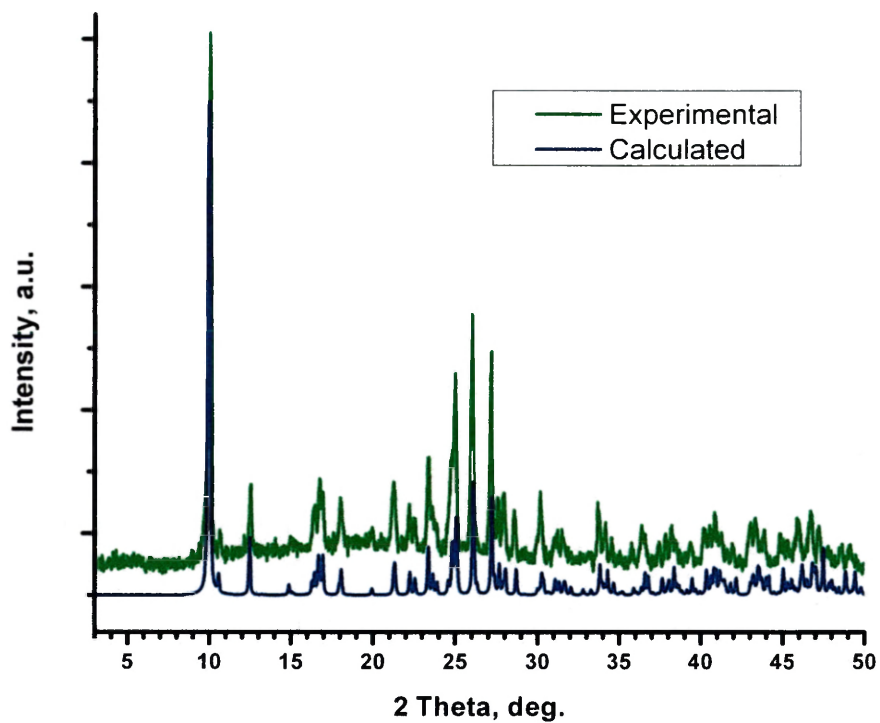


Figure 45. Experimental and calculated PXRD patterns for complex 1

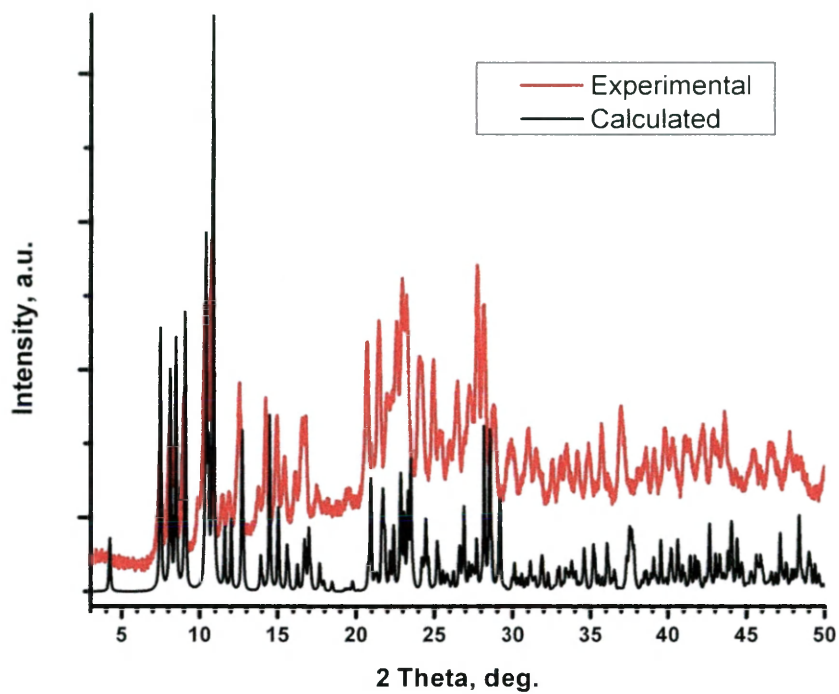


Figure 46. Experimental and calculated PXRD patterns for complex 2

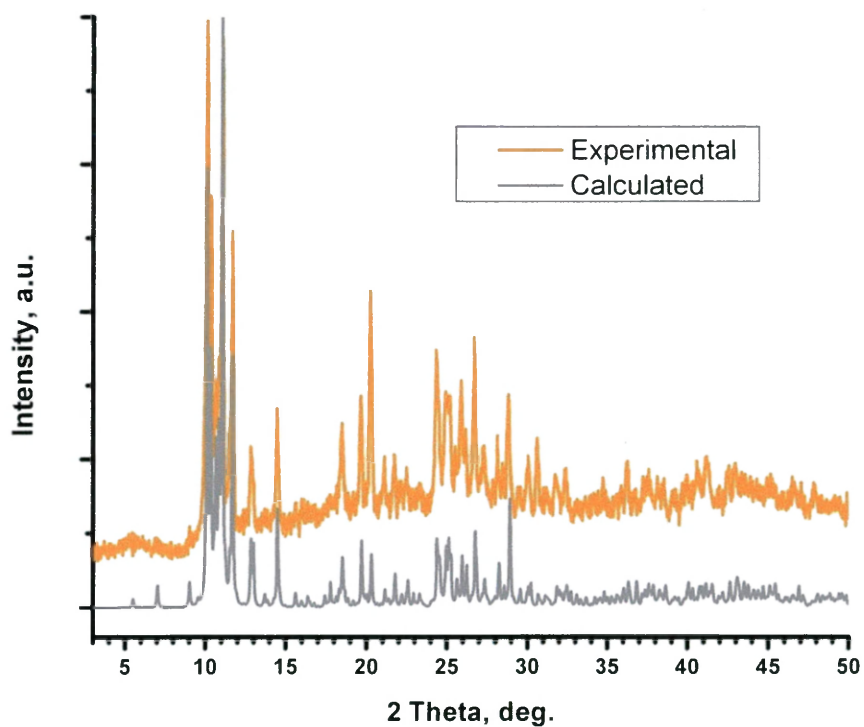


Figure 47. Experimental and calculated PXRD patterns for complex 3a

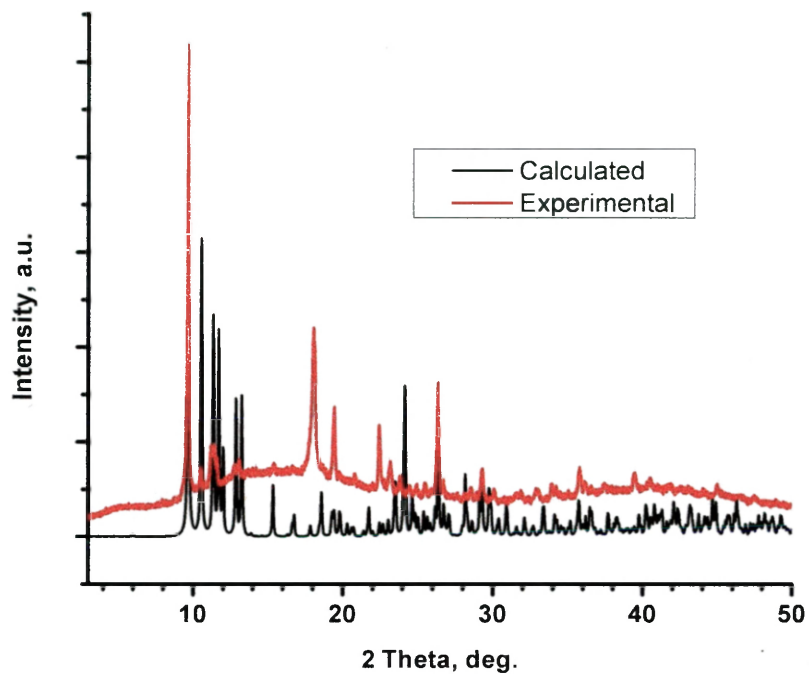


Figure 48. Experimental and calculated PXRD patterns for complex **3b** (ambient temperature, Paratone oil mull, 10 hour scan)

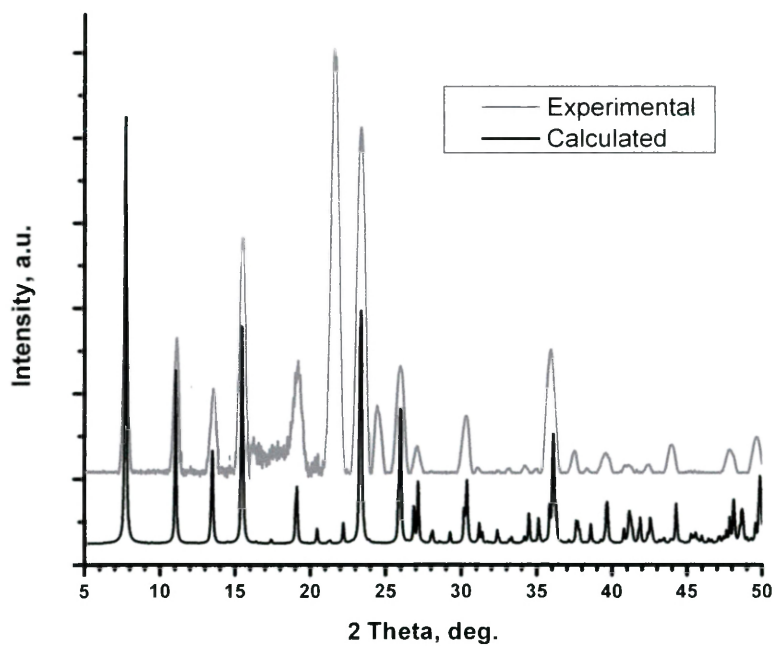


Figure 49. Experimental and calculated PXRD patterns for complex **4** (100 K, Paratone oil mull)

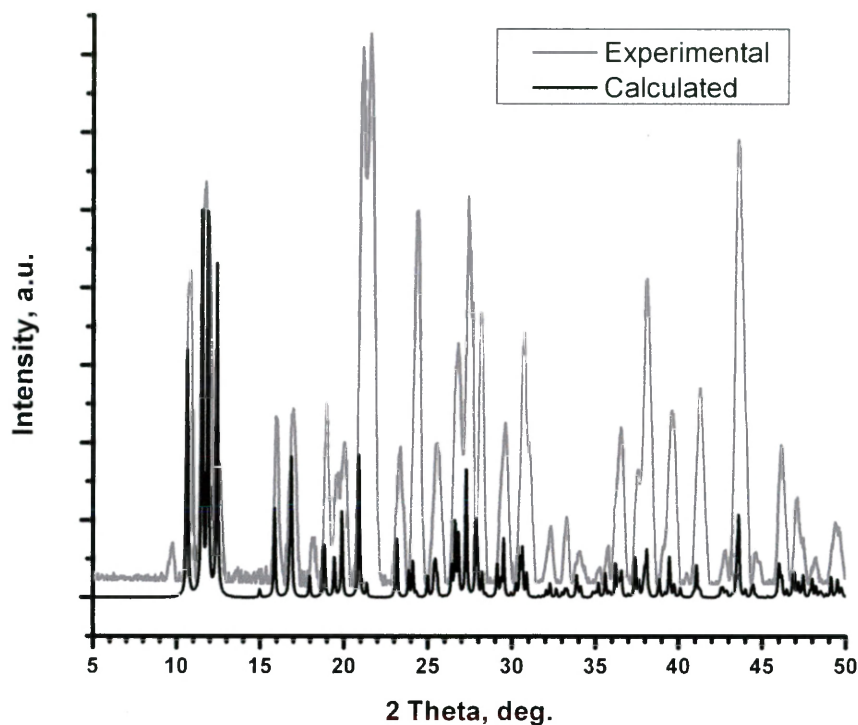


Figure 50. Experimental and calculated PXRD patterns for complex **5** (100 K, Paratone oil mull)

### Thermogravimetric Analysis (TGA) of CuI-THT Powders

TGA was performed on all CuI-THT powders (Figure 51). For all the complexes, the % CuI left after 150 °C corresponded very closely with the theoretical % CuI based on the formula of the complex. The initial mass loss temperatures seen for the various complexes were consistent with the relative stability of the complexes during handling. So, **1**, which was the most stable complex, did not lose any mass until 105 °C. The somewhat less stable **2** and **3a** showed mass losses commencing below 100 °C. Compound **3b** was found to be less stable to heating than its polymorph **3a** by differential scanning calorimetry

(DSC, see below). Thus, **3b** underwent mass loss beginning 30 °C below the analogous point for **3a**. Finally, the least stable compounds **4** and **5** experienced mass loss at very modest temperatures, with a clear MeCN loss step evident for **4**. Carbon and hydrogen chemical analysis was also performed on **1**, **2**, **3a**, and **3b**. The % C and % H for all complexes corresponded well with the theoretical values (see Experimental Section).

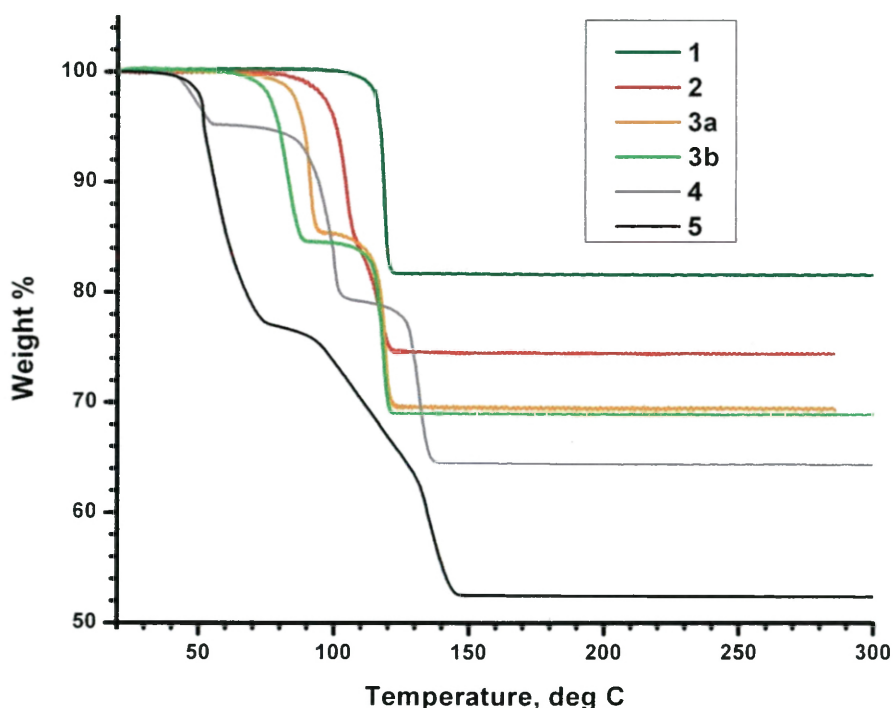


Figure 51. TGA traces of CuI-THT phases.

### Phase Conversion Studies

The interrelationship between the CuI-THT phases was investigated using differential scanning calorimetry (DSC), as well as grinding, vacuum, and low temperature studies. The relationship between **3a** and **3b** was probed first using

DSC. An endothermic transition was apparent for **3b** at 38 °C, as shown in Figure 52. The conversion seen was believed to be from **3b** to **3a**. The conversion from **3a** to **3b** was not observed in the DSC trace since it would require maintaining the sample at temperatures of under 38 °C (Figure 52). So, to confirm this hypothesis, a constant temperature study was performed using heated oil baths. Separate dry samples of **3a** and **3b** were heated in separate vials at 35 and 45 °C. Their luminescent colors were observed in order to determine when a phase conversion had occurred. Over the course of an hour, the dull yellow-emissive **3b** was seen to convert to orange-emissive **3a** at 45 °C, while the **3a** sample remained unchanged. At 35 °C, **3a** converted to **3b**, and **3b** remained unchanged. The transition at 35 °C required overnight heating due to significant activation energy in the solid state. In the stirred crystallization studies in MeCN, **3a** also proved to be the favored polymorph at higher temperatures. The density of **3b** (2.588 g/cm<sup>3</sup>) exceeds that of **3a** (2.461 g/cm<sup>3</sup>). So according to Kitaigorodskii's rule,<sup>69</sup> the more stable complex at room temperature should be **3b**. Both DSC results and controlled-temperature solid state reactions support this assertion. The kinetically-favored polymorph, however appears to be **3a**, based on the results of the grinding studies performed (see below).

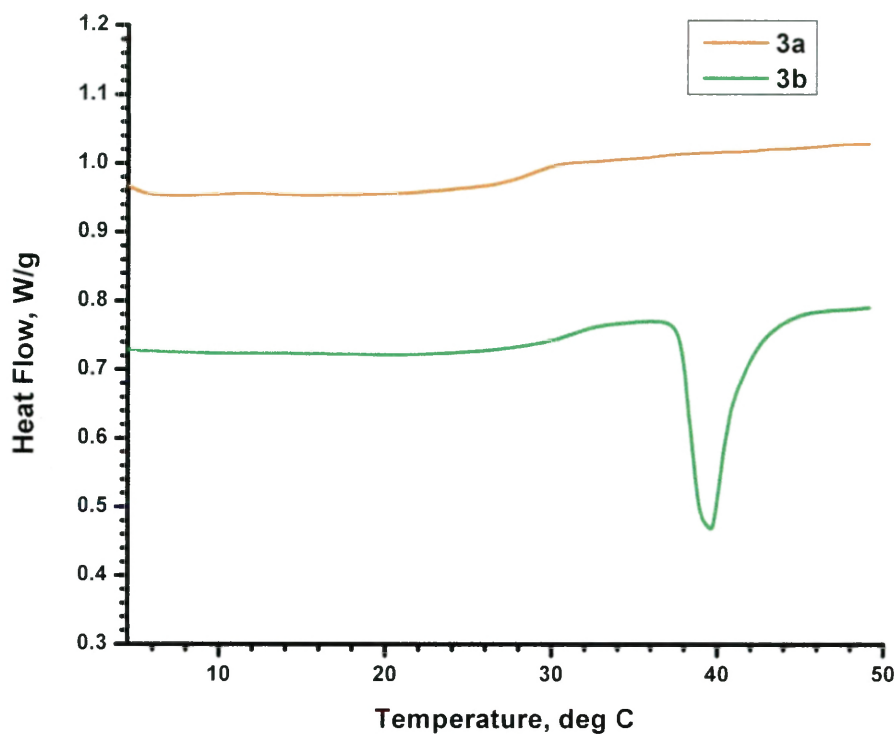


Figure 52. DSC trace for polymorphs **3a** (orange) and **3b** (green).

The mechanochemical conversions of the CuI-THT phases were studied using grinding experiments. Each compound was dry-ground separately. The result was the following set of conversion trends: **1** remained unchanged, **2** converted to **1**, **3a** converted to a **3a/3b** mixture, and **3b** converted to **1**. So, in the absence of THT, the most THT-rich phases convert to the most THT-poor phases by adding mechanical energy. The grindings were also performed in the presence of neat THT. With a sufficient amount of THT present, all phases converted to the most THT-rich phase, **5**. These observations are consistent with the crystallization of **5** from neat THT. The grinding studies also support the facile loss of THT from **5** when left in the air to produce the orange luminescent phase **3a**. Additionally, each compound was placed under vacuum to study their

behavior. Overnight vacuum treatment at 50 mTorr did not affect compounds **1** and **2**. However, both **3a** and **3b** convert to **1**, the most THT-poor phase, under these conditions. The summarized results of the grinding and vacuum study are displayed in Table 7.

Table 7. Grinding and vacuum study results.

Initial Compound	Dry Grinding Product	Grinding Product with Drop of THT	Grinding Product with Excess THT	Vacuum Treatment (50 mTorr)
<b>1</b>	<b>1</b>	<b>3a</b>	<b>5</b>	<b>1</b>
<b>2</b>	<b>1</b>	<b>3a</b>	<b>5</b>	<b>2</b>
<b>3a</b>	<b>3a/3b</b>	<b>3a</b>	<b>5</b>	<b>1</b>
<b>3b</b>	<b>1</b>	<b>3a</b>	<b>5</b>	<b>1</b>

Another phase transition was discovered when crystals of **3a** were cooled on the X-ray diffractometer. Cooling these crystals to 100 K invariably caused them to crack. Thus, an experiment was performed to determine at what temperature the crystals experience the phase transition. A crystal of **3a** was placed on the X-ray goniometer. The instrument was then programmed to collect a single diffraction frame per °C as the crystal was cooled at a rate of 1 °C/min. When the diffraction pattern changed, the temperature was noted. In this work it was discovered that the phase transition occurs at 213 K. The diffraction of this new phase was rendered of lower quality, even after the crystal was warmed back up. The orange emission of **3a** persisted through this phase change, indicating that the new phase was not dull yellow-emissive **3b**. Low temperature



structural determination was not possible for **3a** due to the low quality of the diffraction data, but the unit cell of this new phase (**3a'**) was reliably indexed. A comparison of the unit cell parameters of **3a**, **3a'**, and **3b** is shown in Table 8. The major difference between **3a** and **3a'** is the loss of right angles at lower temperatures, producing a triclinic cell.

Table 8. Unit cell parameters for  $(\text{CuI})_4(\text{THT})_4$  cubane polymorphic phases.

	<b>3a</b>	<b>3a'</b> <sup>a</sup>	<b>3b</b>
<b>Temp., K</b>	250	200	100
<b>Space group</b>	$P2_1/n$	triclinic $P$	$P-1$
<b>a, Å</b>	9.5824(2)	9.69	9.5852(5)
<b>b, Å</b>	34.9161(6)	16.38	10.8359(5)
<b>c, Å</b>	17.9841(3)	36.39	15.7749(8)
<b><math>\alpha</math>, °</b>	90	87.48	73.253(2)
<b><math>\beta</math>, °</b>	91.2810(10)	88.27	72.470(2)
<b><math>\gamma</math>, °</b>	90	88.66	69.213(2)
<b>Volume, Å<sup>3</sup></b>	6015.62(19)	5858	1430.15(12)
<b>Z</b>	8	(8)	2

<sup>a</sup>Limited data set, structure solution not pursued.

### Luminescence Spectroscopy

As shown in Figure 44, four of the CuI-THT phases studied proved to be strongly photoluminescent. The distinct visible emission colors upon irradiation with UV light are of interest because spectroscopic distinctions can reveal differences in the electronic structure of the complexes. Of particular interest is the fact that polymorphs, **3a** and **3b** exhibit different emission wavelengths. Therefore, the luminescent behavior and lifetimes of **1**, **2**, **3a**, and **3a'** were

studied at ambient and liquid nitrogen temperatures. The results are summarized in Table 9 and in Figures 53 and 54. The excitation and emission traces at for each complex are shown in Figure 53 at 293 K and 77 K. From these traces, it is evident that thermochromism is occurring, as well as compound-specific behavior. Figure 54 displays the emission wavelengths of each phase at 77 K. Moderate peak excitation wavelengths resulted for all four complexes (335 – 359 nm). In all cases, the emission seen was at low energies (LE band, 519 – 590). HE bands were uniformly absent due to the fact that THT lacks  $\pi^*$  ligand orbitals needed for XLCT or MLCT.<sup>39, 42–44, 70–71</sup>

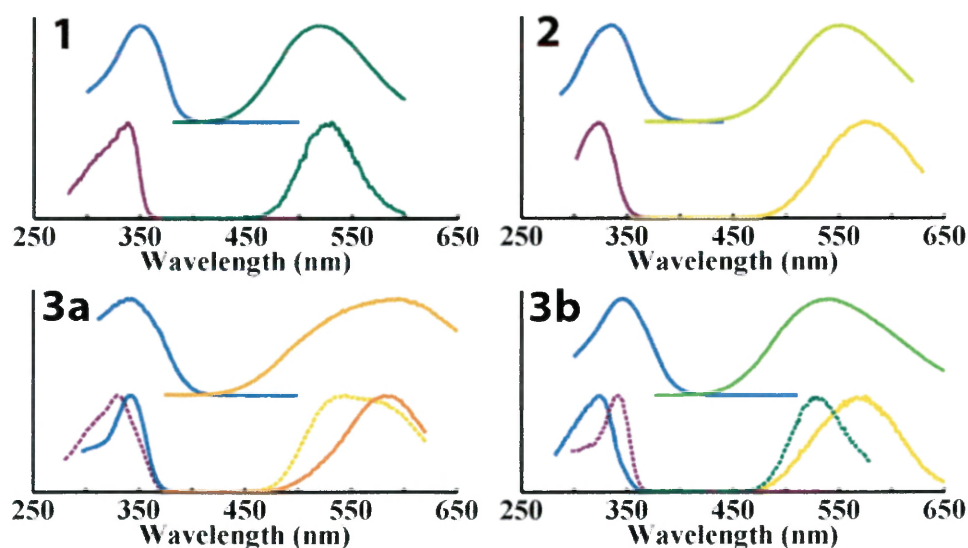


Figure 53. Luminescence spectroscopy of CuI-THT complexes at 293 K (top traces) and 77 K (bottom traces). Excitation wavelength (left) and emission wavelength (right) shown in each case. Dashed/solid line traces indicate linked excitation/emission pairs.

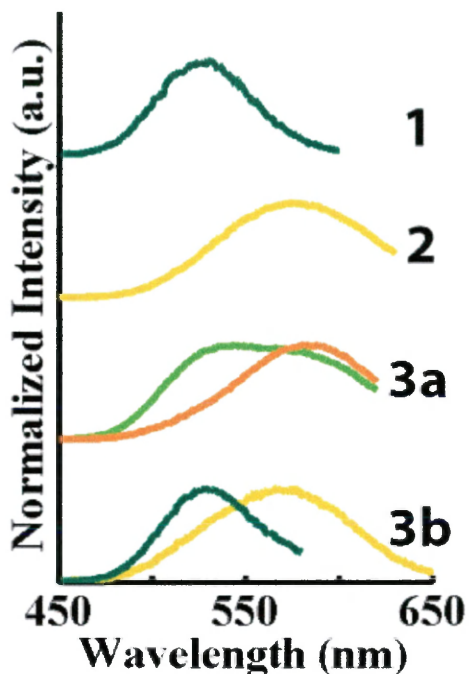


Figure 54. 77 K emission spectra of luminescent CuI-THT complexes.

All complexes studied experienced modest and fully reversible thermochromic effects. Compound **1** showed single excitation and emission bands at 350 nm and 519 nm, respectively. These bands shifted at 77 K to 339 nm and 528 nm. Compound **2** displayed similar behavior with ambient temperature excitation and emission wavelengths at 335 nm and 552 nm, shifting to 330 nm and 575 nm at 77 K. A broad emission band at 590 nm with a peak excitation at 344 nm was observed for compound **3a** at ambient temperature. The broad emission peak and the excitation peak split at 77 K (345/583 nm and 329/545 nm). Compound **3b** showed similar behavior with ambient temperature excitation and emission bands at 346 nm and 541 nm split into two couple excitation/emission band pairs: 341/529 nm and 324/576 nm. As a reminder, compound **3a** is actually at the lower symmetry **3a'** at 77 K. So, the splitting of the

emission bands could be the result of symmetry lowering at reduced temperatures.

Table 9. Luminescence behavior and lifetimes of the CuI-THT complexes.

Compound	T (K)	$\lambda_{em}$ (nm), [ $\lambda_{ex}$ (nm)]	Stokes Shift ( $cm^{-1}$ )	Lifetime ( $\mu s$ )
<b>(CuI)<sub>4</sub>(THT)<sub>2</sub>, 1</b>	293	519, [350]	9,700	12.1
	77	528, [339]	10,600	10.4
<b>(CuI)<sub>10</sub>(THT)<sub>7</sub>(MeCN), 2</b>	293	552, [335]	11,700	23.7
	77	575, [330]	12,900	15.5
<b>(CuI)<sub>4</sub>(THT)<sub>4</sub>, 3a</b>	293	590, [344]	10,200	19.1
	77	583, [345]	12,100	15.0
	77	545, [329]	12,000	9.97
<b>(CuI)<sub>4</sub>(THT)<sub>4</sub>, 3b</b>	293	541, [346]	10,400	6.60
	77	529, [341]	10,400	8.99
	77	576, [324]	13,500	15.5

The compounds exhibit very similar wavelengths, but the subtle differences are instructive. Based on extensive precedent, the LE transitions seen can be attributed to <sup>3</sup>CC behavior. The <sup>3</sup>CC transition is itself a combination of XMCT and MC components according to previous studies.<sup>39, 42-44, 70-71</sup> Three metrics may be used to evaluate the contribution of these components: (1) Stokes shift, (2) thermochromic emission shift, and (3) emission lifetime. A large Stokes shift results because of the distortion of the cluster due to XMCT involving a transition from a largely I-cluster based HOMO to a largely Cu-cluster [(CuI)<sub>n</sub>] based LUMO (n = 2, 4, 6). The increase in degree of bonding, due to excited

state cluster distortion, stabilizes the excited state. The stabilization of the excited state also leads to a longer emission wavelength. A more heavily MC ( $3d^{10} \rightarrow 3d^9 4p^1$ )  $^3CC$  transition would show a lesser degree of Stokes shifting. The lifetimes of  $^3CC$  transitions are typically near 10–20  $\mu\text{s}$ ; in contrast longer lifetimes may be seen due to the more disruptive XMCT.

At reduced temperature, **3a** and **3b** show pairs of excitation/emission bands. For **3b** at 77 K there are differences in the Stokes shift and lifetimes of its pair of coupled bands. The higher energy Stokes shift and longer lifetime (15.5 vs. 8.99  $\mu\text{s}$ ) belong to the lower energy ( $LE_1$ ) 324/576 nm band which has yellow emission. The  $^3CC$  band for the higher energy band ( $LE_2$ ) 341/529 nm, showing green emission, has less  $^3XMCT$  character than the  $LE_1$  band. The longer lifetime can reasonably be associated with the more disruptive  $^3XMCT$  process. Due to the conversion of **3a** discussed previously, **3a'** is the phase considered at 77 K. For **3a'**  $LE_2$  is associated with the lower energy excitation band. The two bands for **3a'** show similar Stokes shifts ( $LE_1 = 12,100$  and  $LE_2 = 12,000 \text{ cm}^{-1}$ ), but different lifetimes ( $LE_1 = 15 \mu\text{s}$  and  $LE_2 = 9.97 \mu\text{s}$ ). Therefore, there appears to be a more even balance between  $^3XMCT$  and  $^3MC$  character in the CC bands for **3a'**. Another compound that shows a relatively high Stokes shift ( $12,900 \text{ cm}^{-1}$ ) and a long lifetime (15.5  $\mu\text{s}$ ) at 77 K is compound **2**. Therefore, it should be regarded as largely  $^3XMCT$  in character. A more modest Stokes shift and a shorter lifetime are observed for compound **1** at 77 K, indicating greater  $^3MC$  character.

## CONCLUSIONS

CuI films were investigated as a potential detector substrate for the detection of VOCs in the air. The optimum film casting method was determined by characterization of the film morphology. The most uniform and consistent films were cast from CuI in MeCN solution using a doctor blade followed by the evaporation of the solvent from the glass cover slip. Film surface morphology was evaluated using optical microscopy and SEM. The vapor-exposed and unexposed films were also compared using PXRD, TGA, and Raman spectroscopy. TGA was determined to be ineffective for determining the presence of surface adducts formed after exposure. The PXRD pattern after exposure was useful for identifying the presence of a new adduct phase. The presence of a CuI-L adduct on the surface of the film was also observed using Raman spectroscopy.

Saturation vapor pressure tests using aromatic amines, aliphatic amine, and sulfides showed a diverse array of photoluminescent adducts on the film surface. The luminescence color varied to some degree with the VOC used, suggesting the potential to differentiate between various VOCs. Partial pressure experiments were conducted on the CuI films, and demonstrated the capability of these films to detect pyridine and 2-methylpyridine down to 21.2 and 20.1 ppm, respectively. The detectable concentrations are not likely to be low enough for CuI to compete with existing sensor technology.

The crystal structures of two previously unknown CuI-halopyridine structures were determined.  $(\text{CuI})_{\infty}(\text{2-bromopyridine})_{\infty}$  and  $(\text{CuI})_{\infty}(\text{2-chloropyridine})_{\infty}$  have a stair step crystal structure motif. The unique CuI-THT system was also investigated. This system is comprised of at least six distinct phases: green-emitting  $(\text{CuI})_4(\text{THT})_2$  (**1**), yellow-emitting  $(\text{CuI})_{10}(\text{THT})_7(\text{MeCN})$  (**2**), orange-emitting  $(\text{CuI})_4(\text{THT})_4$  (**3a**), dull yellow-emitting  $(\text{CuI})_4(\text{THT})_4$  (**3b**), non-emissive  $(\text{CuI})_3(\text{THT})_3 \cdot \text{MeCN}$  (**4**), and non-emissive  $(\text{CuI})_2(\text{THT})_4$  (**5**). Compound **1** is a 3-D network consisting of  $\text{Cu}_4\text{I}_4$  cubane units and  $\mu_2$ -THT ligands. Compound **2** is a 1-D ladder consisting of  $\{[\text{Cu}_4\text{I}_4(\text{THT})](\mu_2\text{-THT})_2(\text{Cu}_2\text{I}_2)(\mu_2\text{-THT})_2[\text{Cu}_4\text{I}_4(\text{NCMe})]\}$  rungs connected by pairs of  $\mu_2$ -THT links. Compounds **3a** and **3b** are simple  $(\text{CuI})_4(\text{THT})_4$  molecules and are polymorphs. Denser triclinic **3b** is more stable than monoclinic **3a** phase at 25 °C, converting to **3a** at  $\geq 38$  °C. **3a** shows a transformation to a triclinic phase (**3a'**) that retains orange emission at -60 °C. Compound **4** is a 2-D sheet containing  $\text{Cu}_3(\text{THT})_3$  rings trigonally linked by rhomboid  $\text{Cu}_2\text{I}_2$  dimer units with MeCN solvent molecules occupying large  $(\text{Cu}_2\text{I}_2)_6(\text{THT})_6$  rings. The dimer **5** consists of a  $\text{Cu}_2\text{I}_2$  rhomboid core decorated with four THT ligands. Increasing temperature of the CuI/THT mixtures in MeCN shows a trend: **4**  $\rightarrow$  **3b**  $\rightarrow$  **3a**  $\rightarrow$  **1**. THT-rich conditions favor **5** while THT-poor conditions favor **1**.

The photoemissive compounds **1**, **2**, **3a**, and **3b** are excited by 335 – 350 nm wavelengths at room temperature and have emission wavelengths from 519 – 590 nm. These bands are attributed to cluster centered transitions which is a combination of halide-to-ligand (XMCT) and metal-centered (MC) components.

At 77 K, both **3a** and **3b** show splitting into coupled pairs of excitation/emission bands. It is hypothesized that the larger Stokes shift and longer lifetime features are a result of greater XMCT character.



## REFERENCES

- <sup>1</sup> EPA, An Introduction to Indoor Air Quality (IAQ), Volatile Organic Compounds (VOCs). <http://www.epa.gov/iaq/voc.html>
- <sup>2</sup> Henderson, R. Gas Detection for VOC Measurement. Occupational Health & Safety. Oct 2004. <http://ohsonline.com/Articles/2004/10/Gas-Detection-for-VOC-Measurement.aspx>
- <sup>3</sup> Wilford, P. VOC Detection and Measurement Techniques, *AWE Magazine* [http://www.awemagazine.com/article.php?article\\_id=519](http://www.awemagazine.com/article.php?article_id=519)
- <sup>4</sup> Wolfrum, E. J.; Meglen, R. M.; Peterson, D.; Sluiter, J. *Sensors and Actuators B* **2006**, 115, 322.
- <sup>5</sup> Macintyre, J. E., ed. Dictionary of Inorganic Compounds, Volume 4, Chapman & Hall, 1992.
- <sup>6</sup> Keen, D. A.; Hull, S. *J. Phys.: Condensed Matter* **1995**, 7, 5793.
- <sup>7</sup> Hull, S.; Keen, D. A.; Hayes, W.; Gardner, N. J. G. *J. Phys. Condensed Matter* **1998**, 10, 10941.
- <sup>8</sup> Hull, S.; Keen, D. A. *Phys. Rev. B* **1994**, 50, 5868.
- <sup>9</sup> Hofmann, M.; Hull, S.; Keen, D. A. *Phys. Rev. B* **1995**, 51, 12022.
- <sup>10</sup> Safko, J. P.; Kuperstock, J. E.; McCullough, S. M.; Noviello, A.M.; Li, X.; Killarney, J. P.; Murphy, C.; Patterson, H. H.; Bayse, C. A.; Pike, R. D. *Dalton Trans* **2012**, 41, 11663.
- <sup>11</sup> Tronic, T. A.; deKrafft, K. E.; Lim, M. J.; Ley, A. N.; Pike, R. D. *Inorg. Chem.* **2007**, 46, 8897.
- <sup>12</sup> Pike, R. D.; deKrafft, K. E.; Ley, A. N.; Tronic, T. A. *Chem. Commun.* **2007**, 3732.
- <sup>13</sup> Lim, M. J.; Murray, C. A.; Tronic, T. A.; deKrafft, K. E.; Ley, A. N.; DeButts, J. C.; Pike, R. D.; Lu, H.; Patterson, H. H. *Inorg. Chem.* **2008**, 47, 6931.
- <sup>14</sup> Ley, A. N.; Dunaway, L. E.; Brewster, T. P.; Dembo, M. D.; Harris, T. D.; Baril-Robert, F.; Li, X.; Patterson, H. H.; Pike, R. D. *Chem. Commun.* **2010**, 46, 4565.
- <sup>15</sup> Dembo, M. D.; Dunaway, L. E.; Jones, J. S.; Lepekhina, E. A.; McCullough, S. M.; Ming, J. L.; Li, X.; Baril-Robert, F.; Patterson, H. H.; Bayse, C. A.; Pike, R. D. *Inorg. Chim. Acta* **2010**, 364, 102.
- <sup>16</sup> Miller, K. M.; McCullough, S. M.; Lepekhina, E. A.; Thibau, I. J.; Pike, R. D. *Inorg. Chem.* **2011**, 50, 7239.
- <sup>17</sup> Kim, T. H.; Shin, Y. W.; Lee, S. S.; Kim, J. *Inorg. Chem. Commun.* **2007**, 10, 11.
- <sup>18</sup> Kim, T. H.; Shin, Y. W.; Jung, J. H.; Kim, J. S.; Kim, J. *Angew. Chem. Int. Ed.* **2008**, 47, 685.
- <sup>19</sup> Xie, C.; Zhou, L.; Feng, W.; Wang, J.; Chen, W. *J. Mol. Struct.* **2009**, 921, 132.
- <sup>20</sup> Zhang, J.; Xue, Y.-S.; Li, Y.-Z.; Du, H.-B.; You, X.-Z. *CrystEngComm* **2011**, 13, 2578.
- <sup>21</sup> Knorr, M. Guyon, F.; Khatyr, A.; Däschlein, C.; Strohmam, C.; Aly, S. M.; Abd-El-Aziz, A. S.; Fortin, D.; Harvey, P. D. *Dalton Trans.* **2009**, 38, 948.
- <sup>22</sup> Knorr, M. Guyon, F.; Kubicki, M. M.; Rousselin, Y.; Aly, S. M.; Harvey, P. D. *New J. Chem.* **2011**, 35, 1184.
- <sup>23</sup> Aly, S. M.; Pam, A.; Khatyr, A.; Knorr, M.; Rousselin, Y.; Kubicki, M. M.; Bauer, J.

- O.; Strohmman, C. D.; Harvey, P. D. *J. Inorg. Organomet. Polym. Mater.* **2014**, in press (DOI: 10.1007/s10904-013-9984-9).
- <sup>24</sup> Paulsson, H.; Berggrund, M.; Fischer, A.; Kloo, L. *Z. Anorg. Allg. Chem.* **2004**, *630*, 413.
- <sup>25</sup> Norén, B.; Oskarsson, Å. *Acta. Chem. Scand. Ser. A* **1987**, *41*, 12.
- <sup>26</sup> Suenaga, Y.; Maekawa, M.; Kuroda-Sowa, T.; Munakata, M.; Morimoto, H.; Hiyama, N.; Kitagawa, S. *Anal. Sci.* **1997**, *13*, 651.
- <sup>27</sup> Heller, M.; Sheldrick, W. S. *Z. Anorg. Allg. Chem.* **2004**, *630*, 1869.
- <sup>28</sup> Lu, W.; Yan, Z.-M.; Dai, J.; Zhang, Y.; Zhu, Q.-Y.; Jia, D.-X.; Guo, W.-J. *Eur. J. Inorg. Chem.* **2005**, 2339.
- <sup>29</sup> Lee, S. Y.; Park, S.; Lee, S. S. *Inorg. Chem.* **2009**, *48*, 11335.
- <sup>30</sup> Jo, M.; Seo, J.; Lindoy, L. F.; Lee, S. S. *Dalton Trans.* **2009**, 6096.
- <sup>31</sup> Martínez-Alanis, P. R.; Ugalde-Saldívar, V. M.; Castillo, I. *Eur. J. Inorg. Chem.* **2011**, 212.
- <sup>32</sup> Boorman, P. M.; Kerr, K. A.; Kydd, R. A.; Moynihan, K. J.; Valentine, K. A. *J. Chem. Soc., Dalton Trans.* **1982**, 1401
- <sup>33</sup> Maelger, H.; Olbrich, F.; Kopf, J.; Abeln, D.; Weiss, E. *Z. Naturforsch. B* **1992**, *47*, 1276.
- <sup>34</sup> Zhou, J.; Bian, G.-Q.; Dai, J.; Zhang, Y.; Zhu, Q.-Y.; Lu, W. *Inorg. Chem.* **2006**, *45*, 8486.
- <sup>35</sup> Filippo, J. S., Jr.; Zyontz, L. E.; Potenza, J. *Inorg. Chem.* **1975**, *14*, 1667.
- <sup>36</sup> Knorr, M.; Pam, A.; Khatyr, A.; Strohmman, C.; Kubicki, M. M.; Rousselin, Y.; Aly, S. M.; Fortin, D.; Harvey, P. D. *Inorg. Chem.* **2010**, *49*, 5834.
- <sup>37</sup> Ford, P. C.; Cariati, E.; Bourassa, J. *Chem. Rev.* **1999**, *99*, 3625.
- <sup>38</sup> Safko, J. P.; Kuperstock, J. E.; McCullough, S. M.; Noviello, A. M.; Li, X.; Killarney, J. P.; Murphy, C.; Patterson, H. H.; Bayse, C. A.; Pike, R. D. *Dalton Trans.* **2012**, *41*, 11663.
- <sup>39</sup> Knorr, M.; Pam, A.; Khatyr, A.; Strohmman, C.; Kubicki, M. M.; Rousselin, Y.; Aly, S. M.; Fortin, D.; Harvey, P. D. *Inorg. Chem.* **2010**, *49*, 5834.
- <sup>40</sup> Vega, A.; Saillard, J.-Y. *Inorg. Chem.* **2004**, *43*, 4012.
- <sup>41</sup> Perruchas, S.; Tard, C.; Le Goff, X. F.; Fargues, A.; Garcia, A.; Kahlal, S.; Saillard, J.-Y.; Gacoin, T.; Boilot, J.-P. *Inorg. Chem.* **2011**, *50*, 10682.
- <sup>42</sup> Liu, Z.; Djurovich, P. I.; Whited, M. T.; Thompson, M. E. *Inorg. Chem.* **2012**, *51*, 230.
- <sup>43</sup> Ford, P. C.; Vogler, A. *Acc. Chem. Res.* **1993**, *26*, 220.
- <sup>44</sup> Ford, P. C. *Coord. Chem. Rev.* **1994**, *132*, 129.
- <sup>45</sup> Hardt, H. D.; Pierre, A. *Z. Anorg. Allg. Chem.* **1973**, *402*, 107.
- <sup>46</sup> Hardt, H. D.; Stoll, H.-J. *Z. Anorg. Allg. Chem.* **1981**, *480*, 193.
- <sup>47</sup> Hardt, H. D.; Stoll, H.-J. *Z. Anorg. Allg. Chem.* **1981**, *480*, 199.
- <sup>48</sup> Raston, C. L.; White, A. H. *J. Chem. Soc., Dalton Trans.* **1976**, 21, 2153.
- <sup>49</sup> Kyle, K. R.; Ryu, C. K.; DiBenedetto, J. A.; Ford, P. C. *J. Am. Chem. Soc.* **1991**, *113*, 2954.
- <sup>50</sup> Perruchas, S.; Tard, C.; LeGoff, X. F.; Fargues, A.; Garcia, A.; Kahlal, S.; Saillard, J.-Y.; Gacoin, T.; Boilot, J.-P. *Inorganic Chemistry* **2011**, *50*, 10682.
- <sup>51</sup> Cariati, E.; Bu, X.; Ford, P. C. *Chem. Mater.* **2000**, *12*, 3385.

- 
- <sup>52</sup> Kauffman, G. B.; Fang, L. Y. *Inorg. Synth.* **1983**, XXII, 101.
- <sup>53</sup> *SMART Apex II, Data Collection Software*, version 2.1; Bruker AXS Inc.: Madison, WI, 2005.
- <sup>54</sup> *SAINT Plus, Data Reduction Software*, version 7.34a; Bruker AXS Inc.: Madison, WI, 2005.
- <sup>55</sup> Sheldrick, G. M. *SADABS*; University of Göttingen: Göttingen, Germany, 2005.
- <sup>56</sup> Altomare, A.; Cascarano, G.; Giacovazzo, C.; Gualardi, A. *J. Appl. Cryst.* **1993**, *26*, 343.
- <sup>57</sup> Sheldrick, G.M. *Acta Crystallogr., Sect. A* **2008**, *64*, 112.
- <sup>58</sup> Hübschle, C. B.; Sheldrick, G. M.; Dittrich, B. *J. Appl. Cryst.* **2011**, *44*, 1281.
- <sup>59</sup> *JADE*, version 6.1 Materials Data Inc. Livermore, CA, 2002.
- <sup>60</sup> *DIFFRAC Plus*, version 10.0 and *EVA*, release 2004; Bruker AXS Inc.: Madison, WI, 2005.
- <sup>61</sup> Macrae, C. F.; Bruno, I. J.; Chisholm, J. A.; Edgington, P. R.; McCabe, P.; Pidcock, E.; Rodriguez-Monge, L.; Taylor, R.; van de Streek, J.; Wood, P. A. *J. Appl. Cryst.* **2008**, *41*, 466.
- <sup>62</sup> Wu, D. Y.; Hayashi, M.; Lin, S. H.; Tian, Z. Q. *Spectrochimica Acta Part A* **2004**, *60*, 137.
- <sup>63</sup> Wu, D.; Hayashi, M.; Shiu, Y.; Liang, K.; Chang, C.; Lin, S. *Journal of the Chinese Chemical Society* **2003**, *50*, 735.
- <sup>64</sup> Lu, J. Y.; Babb, A. M. *Inorg. Chem.* **2002**, *41*, 1339.
- <sup>65</sup> Khalaji, A. D.; Amirasr, M.; Daran, J.-C. *Acta Crystallogr., Sect. E: Struct. Rep. Online* **2006**, *62*, m3222.
- <sup>66</sup> Lu, J. Y.; Babb, A. M. *Inorg. Chem.* **2002**, *41*, 1339.
- <sup>67</sup> Khalaji, A. D.; Amirasr, M.; Daran, J.-C. *Acta Crystallogr., Sect. E: Struct. Rep. Online* **2006**, *62*, m3222.
- <sup>68</sup> Maini, L.; Braga, D.; Mazzeo, P. P.; Ventura, B. *Dalton Trans.* **2012**, *41*, 531.
- <sup>69</sup> Nelyubina, Y. V.; Glukhov, I. V.; Antipin, M. Yu.; Lyssenko, K. A. *Chem. Commun.* **2010**, *46*, 3469
- <sup>70</sup> Vitale, M.; Ford, P. C. *Coord. Chem. Rev.* **2001**, *219–221*, 3.
- <sup>71</sup> Angelis, F. D.; Fantacci, S.; Sgamellotti, A.; Cariati, E.; Ugo, R.; Ford, P. C. *Inorg. Chem.* **2006**, *45*, 10576.